Duhem Modeling of Friction-Induced Hysteresis

ASHWANI K. PADTHE, BOJANA DRINCIC, JINHYOUNG OH, DEMOSTHENIS D. RIZOS, SPILIOS D. FASSOIS, and DENNIS S. BERNSTEIN

EXPERIMENTAL DETERMINATION OF GEARBOX STICTION

Friction is a dynamic phenomenon of widespread importance, and the associated literature is vast; overviews are given in [1]–[5]. Friction can be viewed as an emergent, macroscopic phenomenon arising from molecular interaction. Consequently, both physical (physics-based) and empirical (experiment-based) models have been studied [2], [6]–[14]. Estimation and control methods are available for applications involving friction [15]–[18]; however, these topics are beyond the scope of this article.

Friction models distinguish between *presliding friction* and *sliding friction*. Presliding or *micro-slip* friction refers to the friction forces that occur when the relative displacement between two contacting surfaces is microscopic, that is, on the order of the asperities (roughness features) on the surfaces. Sliding friction refers to the friction forces that arise when the relative displacement is macroscopic. Understanding presliding friction is useful for high precision motion control applications. For example, hysteresis can occur between the presliding friction force input and the displacement output [7], [11], [12].

From a mathematical point of view, friction modeling is challenging since these models often involve nonsmooth dynamics. For example, the most widely used dry friction model, namely, Coulomb friction, is discontinuous. Additional discontinuous dry friction models are studied in [19]. Some friction models are continuous but have non-Lipschitzian dynamics, which is a necessary condition for

finite-settling-time behavior and the associated lack of time-reversibility [20], [21]. Table 1 classifies the properties of some widely used friction models.

Hysteresis is the result of *multistability*, which refers to the existence of multiple attracting equilibria [22]–[24]. Multistability implies that hysteresis is a quasi-static phenomenon in the sense that the hysteresis map is the limit of a sequence of periodic dynamic input-output maps as the period of the input increases without bound. In both presliding and sliding friction models, there exist multiple equilibria corresponding to states that correspond to constant friction forces under constant displacement or velocity.

In this article we examine several classical friction models from a hysteresis modeling point of view and study the
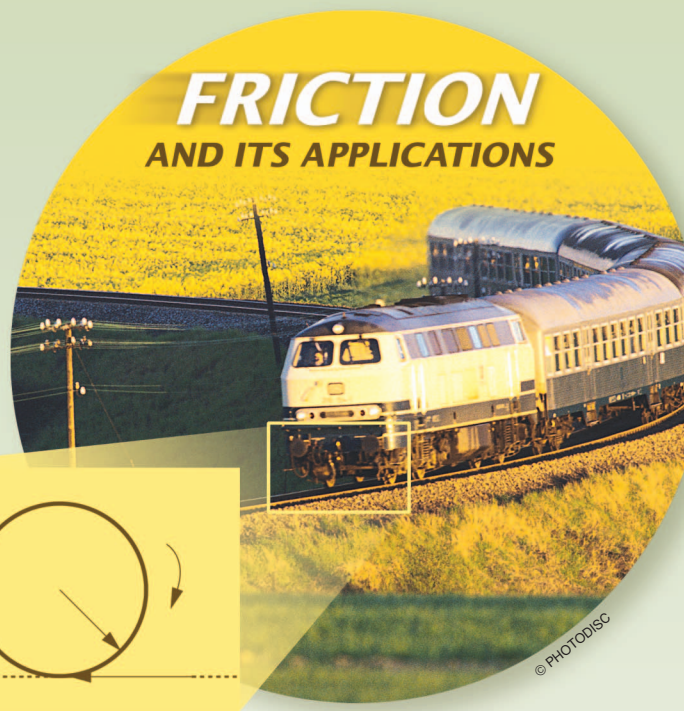
hysteresis induced by these friction models when incorporated into a physical system. Our starting point is [25], which focuses on the Duhem model for hysteresis. For more information on Duhem models, see [26]. The Duhem model has the property that, under constant inputs, every state is an equilibrium. When there exist multiple attracting (step-convergent) equilibria for a given step input, the system exhibits hysteresis under inputs that drive the system through distinct equilibria that map into distinct outputs. In certain cases, the limiting input-output map is independent of the input period; this case is known as *rate-independent* hysteresis. In general, the hysteresis map is *rate dependent*, although the terminology is slightly misleading since, as already noted, hysteresis per se is a quasi-static phenomenon.

The generalized Duhem model $\dot{x} = f(x, u)g(\dot{u})$ and its specialization $\dot{x} = (Ax + Bu)g(\dot{u})$, known as the *semilinear Duhem model*, are considered in [25]. These models give rise to rate-independent hysteresis when the function g is positively homogeneous; otherwise, the hysteresis is generally rate dependent.

In the present article we consider three friction models, namely, the Dahl, LuGre (Lund/Grenoble), and Maxwell-slip models. We recast each model in the form of a generalized or semilinear Duhem model to provide a unified framework for comparing the hysteretic nature of these models. For example, the Dahl model is shown to be a rate-independent generalized Duhem model. Furthermore, in one special case, the Dahl model is also a semilinear Duhem model for which a closed-form solution is available. Similarly, the LuGre model is a rate-dependent generalized Duhem model. Next, we embed each friction model within a single-degree-of-freedom mechanical model to examine and compare the hysteretic response of the combined system.

Finally, we develop an experimental testbed for friction identification. The testbed consists of a dc motor with a speed-reduction gearhead, encoder measurements of the shaft, tachometer measurements of the shaft angular velocity, and load-cell tension measurements of a cable wound around the drum. By operating this testbed under quasi-static conditions, we compare its hysteretic response to the simulated response of the system under various friction models. The goal is to identify a model for the friction and stiction effects observed in the testbed by comparing the simulation and experimental results.

The objective of this article is to reformulate the Dahl, LuGre, and Maxwell-slip models as Duhem models to understand their hysteretic properties. This classification provides the framework for identifying a friction model that captures the hysteretic behavior of the motor gearbox.

The contents of the article are as follows. In the following section we review the basic theory of the Duhem model. Next, we recast the Dahl, LuGre, and Maxwell-slip models as Duhem models and relate their dynamic behavior to properties of the Duhem models. We then study the sliding friction dynamics of the three friction models. Next, we consider friction-induced hysteresis in a mass-spring system. This system is studied as a special case of a linear time-invariant system with Duhem feedback. We then develop a model of the experimental setup and simulate the model using all three friction models. We then report the experimental results and compare them with the simulation results to obtain estimates of the friction parameters. Finally, we give some concluding remarks.

GENERALIZED AND SEMILINEAR DUHEM MODELS

In this section, we summarize the main results of [25] concerning the generalized and semilinear Duhem models. Consider the single-input, single-output *generalized Duhem model*

$$\dot{x}(t) = f(x(t), u(t))g(\dot{u}(t)), \quad x(0) = x_0, \quad t \geq 0, \quad (1)$$

$$y(t) = h(x(t), u(t)), \quad (2)$$

where $x : [0, \infty) \to \mathbb{R}^n$ is absolutely continuous, $u : [0, \infty) \to \mathbb{R}$ is continuous and piecewise C^1, $f : \mathbb{R}^n \times \mathbb{R} \to \mathbb{R}^{n \times r}$ is continuous, $g : \mathbb{R} \to \mathbb{R}^r$ is continuous and satisfies $g(0) = 0$, and $y : [0, \infty) \to \mathbb{R}$, and $h : \mathbb{R}^n \times \mathbb{R} \to \mathbb{R}$ are continuous. The value of $\dot{x}(t)$ at a point t at which $\dot{u}(t)$ does not exist can be assigned arbitrarily. We assume that the solution to (1) exists and is unique on all finite intervals. Under these assumptions, x and y are continuous and piecewise C^1. The terms closed

TABLE 1 Classification and properties of friction models. Each friction model is a Duhem model, with either rate-independent or rate-dependent dynamics. Non-Lipschitzian dynamics is a necessary condition for finite-settling-time convergence.

Friction Model		Duhem Type	Rate Dependence	Continuity
Coulomb		Static	Rate independent	Discontinuous
Dahl	$\gamma = 0$	Generalized	Rate independent	Discontinuous
	$0 < \gamma < 1$	Generalized	Rate independent	Continuous but not Lipschitz
	$\gamma = 1$	Semilinear	Rate independent	Lipschitz
	$\gamma > 1$	Generalized	Rate independent	Lipschitz
LuGre		Generalized	Rate dependent	Lipschitz
Maxwell-slip		Generalized	Rate independent	Discontinuous

curve, limiting periodic input-output map, hysteresis map, and rate independence are defined as follows.

Definition 1
The nonempty set $\mathcal{H} \subset \mathbb{R}^2$ is a closed curve if there exists a continuous, piecewise C^1, and periodic map $\gamma : [0, \infty) \to \mathbb{R}^2$ such that $\gamma([0, \infty)) = \mathcal{H}$.

Definition 2
Let $u : [0, \infty) \to [u_{\min}, u_{\max}]$ be continuous, piecewise C^1, periodic with period α, and have exactly one local maximum $u_{\max}$ in $[0, \alpha)$ and exactly one local minimum $u_{\min}$ in $[0, \alpha)$. For all $T > 0$, define $u_T(t) \triangleq u(\alpha t / T)$, assume that there exists $x_T : [0, \infty) \to \mathbb{R}^n$ that is periodic with period T and satisfies (1) with $u = u_T$, and let $y_T : [0, \infty) \to \mathbb{R}$ be given by (2) with $x = x_T$ and $u = u_T$. For all $T > 0$, the periodic input-output map $\mathcal{H}_T(u_T, y_T, x_0)$ is the closed curve $\mathcal{H}_T(u_T, y_T, x_0) \triangleq \{(u_T(t), y_T(t)) : t \in [0, \infty)\}$, and the limiting periodic input-output map $\mathcal{H}_\infty(u, x_0)$ is the closed curve $\mathcal{H}_\infty(u, x_0) \triangleq \lim_{T \to \infty} \mathcal{H}_T(u_T, y_T, x_0)$ if the limit exists. If there exist $(u, y_1), (u, y_2) \in \mathcal{H}_\infty(u, x_0)$ such that $y_1 \neq y_2$, then $\mathcal{H}_\infty(u)$ is a hysteresis map, and the generalized Duhem model is hysteretic. If, in addition $\mathcal{H}_\infty(u, x_0)$ is independent of x_0 then the generalized Duhem model has local memory, and we write $\mathcal{H}_\infty(u)$. Otherwise, $\mathcal{H}_\infty(u, x_0)$ has nonlocal memory.

Definition 3
The continuous and piecewise C^1 function $\tau : [0, \infty) \to [0, \infty)$ is a positive time scale if $\tau(0) = 0$, τ is nondecreasing, and $\lim_{t \to \infty} \tau(t) = \infty$. The generalized Duhem model (1), (2) is rate independent if, for every pair of continuous and piecewise C^1 functions x and u satisfying (1) and for every positive time scale τ, it follows that $x_\tau(t) \triangleq x(\tau(t))$ and $u_\tau(t) \triangleq u(\tau(t))$ also satisfy (1).

The following result is proved in [25].

Proposition 1
Assume that g is positively homogeneous, that is, $g(\alpha v) = \alpha g(v)$ for all $\alpha > 0$ and $v \in \mathbb{R}$. Then the generalized Duhem model (1), (2) is rate independent.

If g is positively homogeneous, then there exist $h_+, h_- \in \mathbb{R}^r$ such that

$$g(v) = \begin{cases} h_+ v, & v \geq 0, \\ h_- v, & v < 0, \end{cases} \quad (3)$$

and the rate-independent generalized Duhem model (1), (2) can be reparameterized in terms of u [25]. Specifically, consider

$$\frac{d\hat{x}(u)}{du} = \begin{cases} f_+(\hat{x}(u), u), & \text{when } u \text{ increases,} \\ f_-(\hat{x}(u), u), & \text{when } u \text{ decreases,} \\ 0, & \text{otherwise,} \end{cases} \quad (4)$$

$$\hat{y}(u) = h(\hat{x}(u), u), \quad (5)$$

for $u \in [u_{\min}, u_{\max}]$ and with initial condition $\hat{x}(u_0) = x_0$, where $f_+(x, u) \triangleq f(x, u)h_+$, $f_-(x, u) \triangleq f(x, u)h_-$, and $u_0 \in [u_{\min}, u_{\max}]$. Then $x(t) \triangleq \hat{x}(u(t))$ and $y(t) \triangleq \hat{y}(u(t))$ satisfy (1), (2). Note that the reparameterized Duhem model (4) and (5) can be viewed as a time-varying dynamical system with nonmonotonic time u.

As a specialization of (1) and (2), we now consider the *rate-independent semilinear Duhem model*

$$\begin{aligned} \dot{x}(t) = &[\dot{u}_+(t)I_n \quad \dot{u}_-(t)I_n] \\ &\times \left(\begin{bmatrix} A_+ \\ A_- \end{bmatrix} x(t) + \begin{bmatrix} B_+ \\ B_- \end{bmatrix} u(t) + \begin{bmatrix} E_+ \\ E_- \end{bmatrix} \right), \end{aligned} \quad (6)$$

$$y(t) = Cx(t) + Du(t), \qquad x(0) = x_0, \quad t \geq 0, \quad (7)$$

where $A_+ \in \mathbb{R}^{n \times n}$, $A_- \in \mathbb{R}^{n \times n}$, $B_+ \in \mathbb{R}^n$, $B_- \in \mathbb{R}^n$, $E_+ \in \mathbb{R}^n$, $E_- \in \mathbb{R}^n$, $C \in \mathbb{R}^{1 \times n}$, $D \in \mathbb{R}$, and

$$\dot{u}_+(t) \triangleq \max\{0, \dot{u}(t)\}, \quad \dot{u}_-(t) \triangleq \min\{0, \dot{u}(t)\}. \quad (8)$$

Let $\rho(A)$ denote the spectral radius of $A \in \mathbb{R}^{n \times n}$ and let the *limiting input-output map* $\mathcal{F}_\infty(u, y)$ be the set of points $z \in \mathbb{R}^2$ such that there exists an increasing, divergent sequence $\{t_i\}_{i=1}^\infty$ in $[0, \infty)$ satisfying

$$\lim_{i \to \infty} \|(u(t_i), y(t_i)) - z\| = 0.$$

The following result given in [25] provides a sufficient condition for the existence of the limiting periodic input-output map for the rate-independent semilinear Duhem model.

Theorem 1
Consider the rate-independent semilinear Duhem model (6), (7), where $u : [0, \infty) \to [u_{\min}, u_{\max}]$ is continuous, piecewise C^1, and periodic with period α and has exactly one local maximum $u_{\max}$ in $[0, \alpha)$ and exactly one local minimum $u_{\min}$ in $[0, \alpha)$. Furthermore, define $\beta \triangleq u_{\max} - u_{\min}$, and assume that

$$\rho(e^{\beta A_+} e^{-\beta A_-}) < 1. \quad (9)$$

Then, for all $x_0 \in \mathbb{R}^n$, (6) has a unique periodic solution $x : [0, \infty) \to \mathbb{R}^n$, and the limiting periodic input-output map $\mathcal{H}_\infty(u, x_0)$ exists. Specifically, if A_+ and A_- are invertible, then

$$\begin{aligned} \mathcal{H}_\infty(u) = &\{(u, \hat{y}_+(u)) \in \mathbb{R}^2 : u \in [u_{\min}, u_{\max}]\} \\ &\cup \{(u, \hat{y}_-(u)) \in \mathbb{R}^2 : u \in [u_{\min}, u_{\max}]\}, \quad (10) \end{aligned}$$

where

$$\begin{aligned} \hat{y}_+(u) = Ce^{A_+(u-u_{\min})}\hat{x}_+ - C\mathcal{Z}_+(u, u_{\min}) + Du, \\ \hat{y}_-(u) = Ce^{A_-(u-u_{\max})}\hat{x}_- - C\mathcal{Z}_-(u, u_{\max}) + Du, \end{aligned}$$

and

$$\hat{x}_+ \triangleq -(I - e^{-\beta A_-}e^{\beta A_+})^{-1}(e^{-\beta A_-}\mathcal{Z}_+(u_{\max}, u_{\min})$$
$$+ \mathcal{Z}_-(u_{\min}, u_{\max})),$$
$$\hat{x}_- \triangleq -(I - e^{\beta A_+}e^{-\beta A_-})^{-1}(e^{\beta A_+}\mathcal{Z}_-(u_{\min}, u_{\max})$$
$$+ \mathcal{Z}_+(u_{\max}, u_{\min})),$$
$$\mathcal{Z}_+(u, u_0) \triangleq A_+^{-1}(uI - u_0 e^{A_+(u-u_0)})B_+$$
$$+ A_+^{-2}(I - e^{A_+(u-u_0)})B_+ + A_+^{-1}(I - e^{A_+(u-u_0)})E_+,$$
$$\mathcal{Z}_-(u, u_0) \triangleq A_-^{-1}(uI - u_0 e^{A_-(u-u_0)})B_-$$
$$+ A_-^{-2}(I - e^{A_-(u-u_0)})B_- + A_-^{-1}(I - e^{A_-(u-u_0)})E_-.$$

See [25] for the case in which A_+ or A_- is singular.

Definition 2 and Theorem 1 imply that the rate-independent semilinear Duhem model has local memory since the hysteresis map $\mathcal{H}_\infty(u)$ given by (10) is independent of the initial condition $x_0 \in \mathbb{R}^n$.

FRICTION MODELS

Dahl Model

The Dahl model [6], [27], [28] has the form

$$\dot{F}(t) = \sigma \left| 1 - \frac{F(t)}{F_C}\mathrm{sgn}\,\dot{u}(t) \right|^\gamma \mathrm{sgn}\left(1 - \frac{F(t)}{F_C}\mathrm{sgn}\,\dot{u}(t)\right)\dot{u}(t),$$

$$(11)$$

where F is the friction force, u is the relative displacement between the two surfaces in contact, $F_C > 0$ is the Coulomb friction force, $\gamma \geq 0$ is a parameter that determines the shape of the force-deflection curve (as represented by a plot of the friction force versus the relative displacement), and $\sigma > 0$ is the rest stiffness, that is, the slope of the force-deflection curve when $F = 0$. The right-hand side of (11) is Lipschitz continuous in F for $\gamma \geq 1$ but not Lipschitz continuous in F for $0 \leq \gamma < 1$.

When u is increasing, $\dot{F}(t)$ given by (11) is positive for all $F(t) < F_C$ and negative for all $F(t) > F_C$. Similarly, when u is decreasing, $\dot{F}(t)$ given by (11) is positive for all $F(t) < -F_C$ and negative for all $F(t) > -F_C$. Hence the magnitude of the friction force $F(t)$ approaches F_C under monotonic inputs. As shown in Figure 1, the parameter γ determines the shape of the hysteresis map. In practice, γ is typically set to zero or one. As shown in Figure 2, the friction force given by the Dahl model lags the friction force given by the Coulomb model when the direction of motion is reversed.

To represent (11) as a Duhem model, let

$$\mathcal{D}_+(F) \triangleq \sigma \left| 1 - \frac{F}{F_C} \right|^\gamma \mathrm{sgn}\left(1 - \frac{F}{F_C}\right), \qquad (12)$$

$$\mathcal{D}_-(F) \triangleq \sigma \left| 1 + \frac{F}{F_C} \right|^\gamma \mathrm{sgn}\left(1 + \frac{F}{F_C}\right). \qquad (13)$$
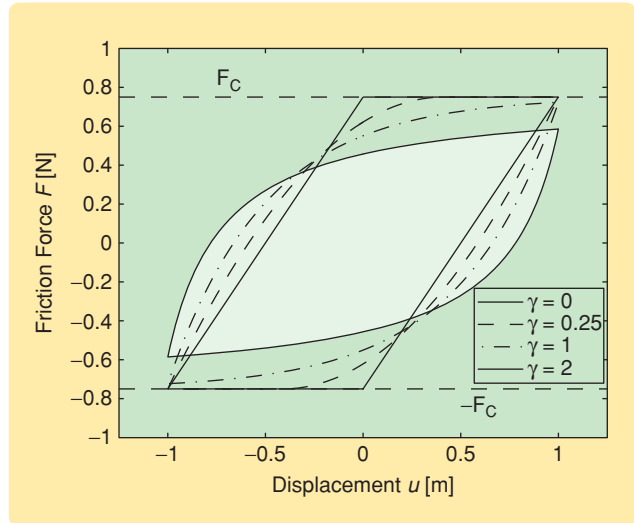
Then the Dahl model (11) can be rewritten as

FIGURE 1 Displacement u versus friction force F for hysteresis maps of the Dahl model for several values of γ. The shape of the hysteresis map from u to F depends on the value of γ. The numerical values used are $F_C = 0.75$ N, $\sigma = 1.5$ N/m, and $u(t) = \sin 0.1t$ m.
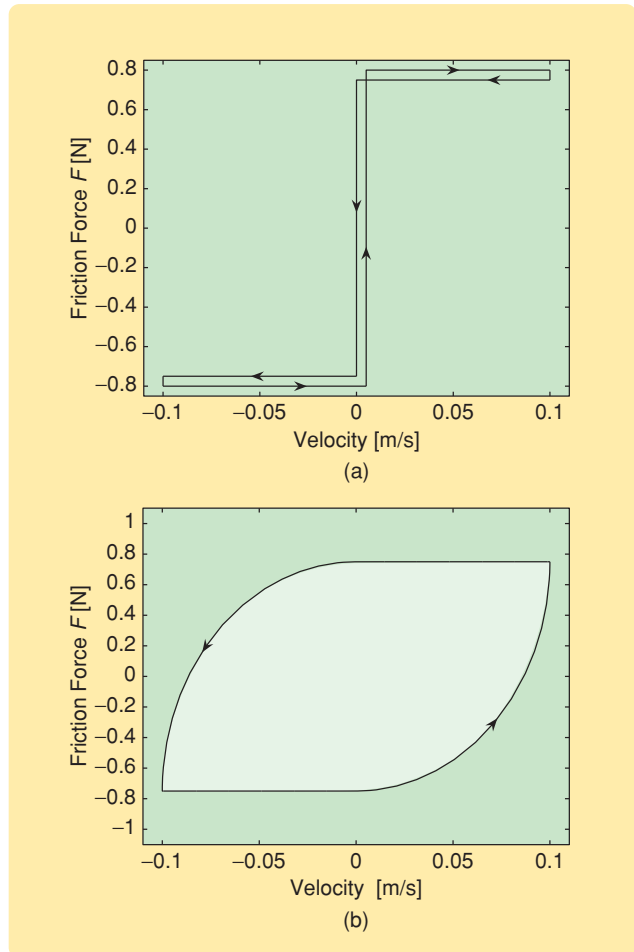

FIGURE 2 Velocity $\dot{u}$ versus friction force F for (a) the Coulomb model (with the traversals offset for clarity) and (b) the Dahl model with $\gamma = 0$. The friction force of the Dahl model lags the friction force of the Coulomb model when $\dot{u}$ changes sign.

$$\dot{F}(t) = \sigma \left[\mathcal{D}_+(F(t)) \quad \mathcal{D}_-(F(t)) \right]$$
$$\times \begin{bmatrix} \dot{u}_+(t) \\ \dot{u}_-(t) \end{bmatrix}, \tag{14}$$
$$y = F, \tag{15}$$

which, for all $\gamma \geq 0$, is a generalized Duhem model of the form (1), (2). Furthermore, since $g(\dot{u}) = [\dot{u}_+(t) \quad \dot{u}_-(t)]^{\mathrm{T}}$ is positively homogeneous, Proposition 1 implies that (14) is rate independent for all $\gamma \geq 0$.

Let $\gamma = 1$. Then (11) becomes

$$\dot{F}(t) = \sigma \left(1 - \frac{F(t)}{F_{\mathrm{C}}} \mathrm{sgn}\, \dot{u}(t) \right) \dot{u}(t)$$
$$= \left[-\frac{\sigma}{F_{\mathrm{C}}} F(t) + \sigma \quad \frac{\sigma}{F_{\mathrm{C}}} F(t) + \sigma \right] \begin{bmatrix} \dot{u}_+(t) \\ \dot{u}_-(t) \end{bmatrix},$$

which is a rate-independent semilinear Duhem model. Furthermore, the convergence condition (9) becomes

$$e^{-2\frac{\beta\sigma}{F_{\mathrm{C}}}} < 1, \tag{16}$$

which holds if and only if $\beta > 0$. As a direct consequence of Theorem 1, which explicitly characterizes the hysteresis map, we have the following result. The corresponding hysteresis map is shown in Figure 1.

Corollary 1

Consider the Dahl model (11) with $\gamma = 1$. Let $u : [0, \infty) \to [u_{\min}, u_{\max}]$ be continuous, piecewise C^1, and periodic with period α and have exactly one local maximum $u_{\max}$ in $[0, \alpha)$ and exactly one local minimum $u_{\min}$ in $[0, \alpha)$. Then (16) holds, and (14), (15) has a unique periodic solution $F : [0, \infty) \to \mathbb{R}^n$, and, for all $x_0 \in \mathbb{R}^n$, the limiting periodic input-output map $\mathcal{H}_\infty(u)$ exists. Furthermore,

$$\mathcal{H}_\infty(u) = \left\{ (u, \hat{F}_+(u)) \in \mathbb{R}^2 : u \in [u_{\min}, u_{\max}] \right\}$$
$$\cup \left\{ (u, \hat{F}_-(u)) \in \mathbb{R}^2 : u \in [u_{\min}, u_{\max}] \right\}, \tag{17}$$

where

$$\hat{F}_+(u) \triangleq e^{-\frac{\sigma}{F_{\mathrm{C}}}(u - u_{\min})} \hat{\alpha}_+ + F_{\mathrm{C}} \left(1 - e^{-\frac{\sigma}{F_{\mathrm{C}}}(u - u_{\min})} \right),$$
$$\hat{F}_-(u) \triangleq e^{\frac{\sigma}{F_{\mathrm{C}}}(u - u_{\max})} \hat{\alpha}_- - F_{\mathrm{C}} \left(1 - e^{-\frac{\sigma}{F_{\mathrm{C}}}(u - u_{\max})} \right),$$

and

$$\hat{\alpha}_+ = -\hat{\alpha}_- = F_{\mathrm{C}} \frac{e^{\frac{-\beta\sigma}{F_{\mathrm{C}}}} - 1}{e^{-\frac{\beta\sigma}{F_{\mathrm{C}}}} + 1}.$$

Corollary 1 implies that the Dahl model (11) with $\gamma = 1$ has local memory since it is a rate-independent semilinear Duhem model and $\mathcal{H}_\infty(u)$ defined by (17) is independent of x_0.

LuGre Model

The LuGre model [10], which models the asperities of two surfaces as elastic bristles, is given by

$$\dot{x}(t) = \dot{u}(t) - \frac{|\dot{u}(t)|}{r(\dot{u}(t))} x(t), \tag{18}$$
$$F(t) = \sigma_0 x(t) + \sigma_1 \dot{x}(t) + \sigma_2 \dot{u}(t), \tag{19}$$

where x is the average deflection of the bristles, u is the relative displacement, F is the friction force, and $\sigma_0, \sigma_1, \sigma_2 > 0$ are stiffness, damping, and viscous friction coefficients, respectively. The right-hand side of (18) is Lipschitz continuous with respect to x. In [1] and [10], $r(\dot{u}(t))$ is defined by

$$r(\dot{u}(t)) = \frac{F_{\mathrm{C}}}{\sigma_0} + \frac{F_{\mathrm{S}} - F_{\mathrm{C}}}{\sigma_0} e^{-(\dot{u}(t)/v_{\mathrm{S}})^2}, \tag{20}$$

where $F_{\mathrm{C}} > 0$ is the Coulomb friction force, F_{S} is the stiction (sticking friction) force, and v_{S} is the Stribeck velocity.

For a given constant velocity $\dot{u}$, the steady-state friction force F_{ss} obtained from (18) and (19) is

$$F_{\mathrm{ss}}(\dot{u}) = \sigma_0 r(\dot{u}) \mathrm{sgn}(\dot{u}) + \sigma_2 \dot{u}. \tag{21}$$

The drop in friction force (see Figure 3) at low magnitudes of velocity is due to the Stribeck effect, while the Stribeck velocity is the velocity at which the steady-state friction force begins to decrease when the velocity is positive and increasing. The LuGre model (18), (19) combines the friction lag of the Dahl model with the Stribeck effect [10], [29].

Letting $F_{\mathrm{S}} = F_{\mathrm{C}}$ in (20) and $\sigma_1 = \sigma_2 = 0$ in 19, the LuGre model (18), (19), (20) is equivalent to the Dahl model (11)

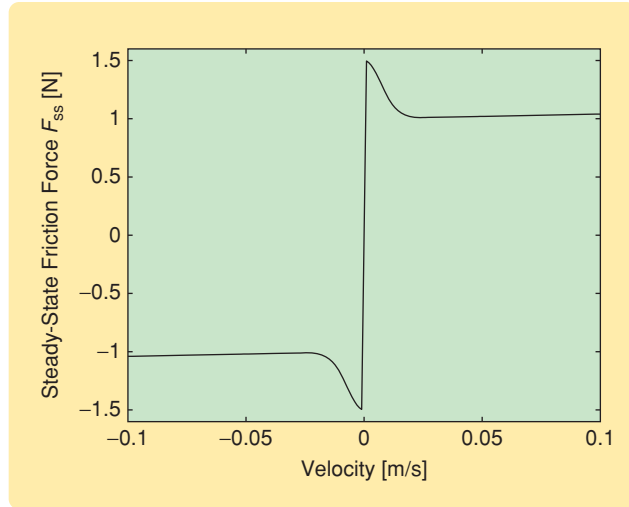**FIGURE 3** Steady-state friction force (21) given by the LuGre model. The drop in the friction force at low velocities is the Stribeck effect, while the Stribeck velocity $v_{\mathrm{S}} = 0.001$ m/s is the velocity at which the steady-state friction force begins to decrease when the velocity is positive and increasing. The numerical values are $F_{\mathrm{C}} = 1$ N, $F_{\mathrm{S}} = 1.5$ N, $v_{\mathrm{S}} = 0.001$ m/s, $\sigma_0 = 10^5$ N/m, $\sigma_1 = \sqrt{10^5}$ N-s/m, and $\sigma_2 = 0.4$ N-s/m.

with $\gamma = 1$ and $\sigma = 1$. With $y = F$, the state equations (18) and (19) can be written as

$$\dot{x}(t) = \begin{bmatrix} 1 & x(t) \end{bmatrix} \begin{bmatrix} \dot{u}(t) \\ -\frac{|\dot{u}(t)|}{r(\dot{u}(t))} \end{bmatrix}, \qquad (22)$$

$$y(t) = \sigma_0 x(t) + \sigma_1 \dot{x}(t) + \sigma_2 \dot{u}(t), \qquad (23)$$

which is a generalized Duhem model of the form (1). Since r given in (20) is not a positively homogeneous function of $\dot{u}$, the LuGre model is not necessarily rate independent. In fact, the input-output maps in Figure 4 show that the LuGre model is rate dependent.

As noted in [30] and [31] the LuGre model has local memory. Thus the hysteresis map $\mathcal{H}_\infty(u, x_0)$ of the LuGre model is independent of x_0.

Maxwell-Slip Model

The Maxwell-slip model [7], [12], [13] shown in Figure 5 has N masses and N springs. For $i = 1, \ldots, N$, the mass m_i with displacement x_i is connected by a stiffness k_i to a common termination point whose displacement is u. Associated with each mass is a displacement deadband of width $\Delta_i > 0$, below which the mass does not move, and above which the mass moves with velocity $\dot{u}$, that is, the inertia of the masses is ignored when the mass is sliding. Hence, $k_i \Delta_i$ is the minimum spring force needed to move the mass m_i. Once the mass m_i begins to move, the spring force remains at $k_i \Delta_i$ for all velocities of the mass. Hence, each mass-spring combination in the Maxwell-slip model is subjected to an equivalent Coulomb friction force $F = k_i \Delta_i$.

We can represent this system as the Duhem model

$$\dot{x}_i(t) = [U(-x_i(t) + u(t) - \Delta_i) \quad 1 - U(-x_i(t) + u(t) + \Delta_i)] \begin{bmatrix} \dot{u}_+(t) \\ \dot{u}_-(t) \end{bmatrix}, \qquad (24)$$

$$F(t) = \sum_{i=1}^{N} k_i(-x_i(t) + u(t)), \quad i = 1, \ldots, N, \qquad (25)$$

where F is the friction force and

$$U(v) \triangleq \begin{cases} 1, & v \geq 0, \\ 0, & v < 0. \end{cases} \qquad (26)$$

The Maxwell-slip model (24), (25) is a generalized Duhem model of the form (1), (2). Since $[\dot{u}_+(t) \quad \dot{u}_-(t)]^T$ is positively homogeneous, Proposition 1 implies that (24), (25) is rate independent. Since the step function U is discontinuous, the Maxwell-slip model is discontinuous.

Illustrative input-output maps for the Maxwell-slip model for $N = 1$ and $N = 10$ are shown in Figure 6(a) and (b), respectively.

Consider the ith mass-spring element in the Maxwell-slip model. If the deflection $x_i - u$ of the spring is less than Δ_i, then m_i does not move, that is, $x_i = 0$, and the friction force due to the ith element is given by $F = k_i u$ and thus
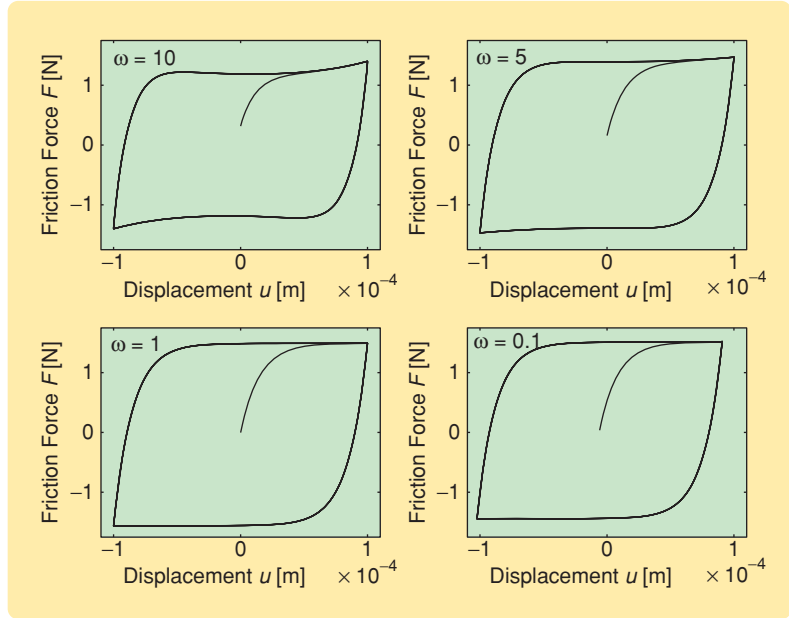

FIGURE 4 Input-output maps for the LuGre model. This sequence of input-output maps at increasingly lower frequencies shows that rate-dependent hysteresis exists from the relative displacement u to the friction force F. The numerical values are $F_C = 1$ N, $F_S = 1.5$ N, $v_S = 0.001$ m/s, $\sigma_0 = 10^5$ N/m, $\sigma_1 = \sqrt{10^5}$ N-s/m, $\sigma_2 = 0.4$ N-s/m, and $u(t) = 10^{-4} \sin \omega t$ m.
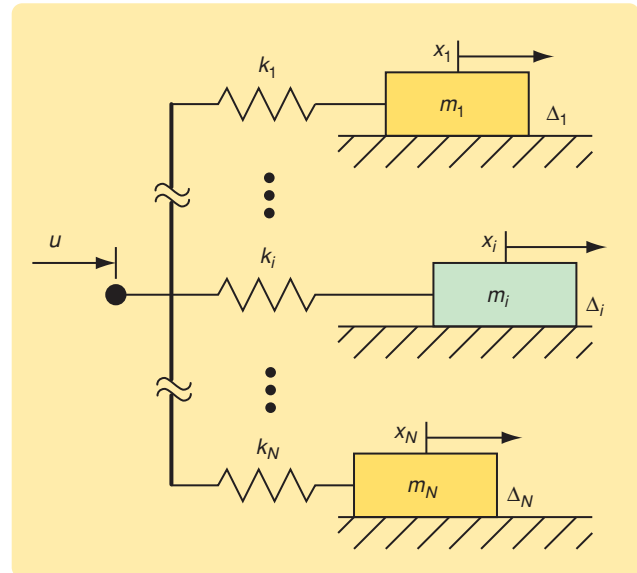

FIGURE 5 The Maxwell-slip model with N masses and N springs. Each mass is associated with a displacement deadband Δ_i, below which the mass does not move and above which the mass moves with the same velocity as the common termination point.

$\dot{F} = k_i \dot{u}$. If the deflection is equal to Δ_i, then $\dot{x}_i = \dot{u}$, and hence $F = k_i \Delta_i$ and thus $\dot{F} = 0$. Consequently, each mass-spring combination in the Maxwell-slip model is a Dahl model with $\gamma = 0$ and $\sigma = k_i$, which has the form

$$\dot{F}(t) = k_i \left[\text{sgn}\left(1 - \frac{F(t)}{F_C} \text{sgn } \dot{u}(t)\right) \right] \dot{u}(t).$$
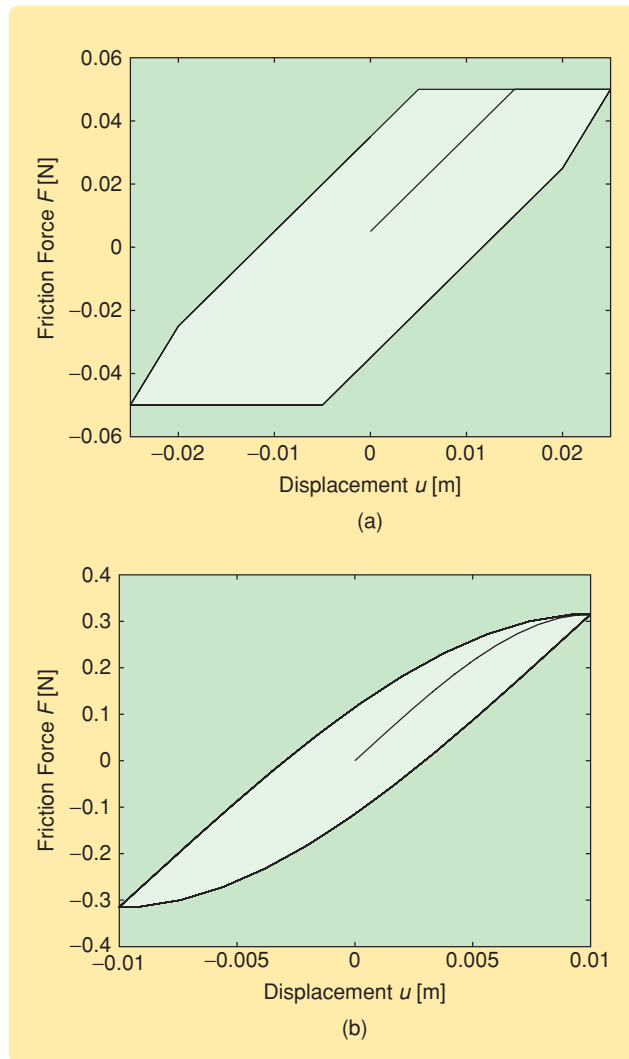

(a)

(b)

FIGURE 6 Input-output maps for the Maxwell-slip model (a) with $N = 2$, $\Delta_1 = [2.5, 15] \times 10^{-3}$ m, $k = [2, 3]$ N/m, and $u(t) = 0.01 \sin 0.1t$ m, and (b) with $N = 10$, $\Delta = [1.5, 2.4, 3.3, 4.2, 5.1, 6, 6.9, 7.8, 8.7, 9.6] \times 10^{-3}$ m, $k = [1, 1.8, 2.6, 3.4, 4.2, 5, 5.8, 6.6, 7.4, 8.2]$ N/m, and $u(t) = 0.01 \sin 0.1t$ m. The maps show hysteresis from the displacement u to the friction force F.

The Maxwell-slip model has nonlocal memory. Consider (24), (25) with $N = 2$ and $N = 10$ shown in Figure 7(a) and (b), respectively. The input $u(t)$ is initially $u_1(t) = 0.025 \sin(0.1t)$ m in Figure 7(a) and $u_1(t) = 0.01 \sin(0.1t)$ m in Figure 7(b), while the friction force corresponds to the major loops in (a) and (b). When $u(t)$ changes to $u_2(t) = 0.005 \sin(0.1t)$ m after one period, the friction force F corresponds to the upper minor loops in Figure 7(a) and (b). When $u(t)$ changes to $u_2(t)$ after one and a half periods, F corresponds to the lower minor loops in Figure 7(a) and (b). Consequently, with identical inputs but different initial conditions, (24), (25) result in distinct hysteresis maps for the same input $u(t)$. Thus, $\mathcal{H}_\infty(u, x_0)$ depends on x_0, and the Maxwell-slip model has nonlocal memory.

SLIDING BEHAVIOR OF THE FRICTION MODELS
We now consider the behavior of the presliding friction models in the sliding regime, that is, the behavior of these models when subject to large-magnitude displacement and velocity.

Dahl Model
Consider the Dahl model (11) with $\gamma = 1$. The friction force F as a function of displacement u and velocity $\dot{u}$ is shown in Figure 8, where u and $\dot{u}$ are initially set to zero. The position is -20 m when the sign of the velocity changes from negative to positive, and is 0 m when the sign of the velocity changes from positive to negative.

As mentioned above, Figure 8(b) shows that each velocity reversal leads to a delayed change in the sign of the friction force.

LuGre Model
The friction force F as a function of displacement u and velocity $\dot{u}$ for the LuGre model is shown in Figure 9. The Stribeck effect causes the friction force to drop at low magnitudes of velocity.

Maxwell-Slip Model
The friction force F as a function of displacement u and velocity $\dot{u}$ for the Maxwell-slip model is shown in Figure 10. The behavior is similar to that of the Dahl model, that is, sign reversals of the friction force lag velocity sign changes.

ENERGY DISSIPATION DUE TO FRICTION
The energy dissipated during one cycle of motion of a mechanical system in periodic motion is equal to the area enclosed by the counterclockwise force-displacement loop. Since the hysteresis in a friction model occurs between the

friction force and the relative displacement of the surfaces, the area enclosed by the hysteresis map is approximately equal to the kinetic energy lost due to friction at low frequencies. If the hysteresis is rate independent, then the area enclosed by the hysteresis map is equal to the energy dissipated during one cycle of operation at all frequencies.

Dahl Model

Consider the Dahl model (11) with $\gamma = 1$. In this case, the hysteresis map shown in Figure 1 encloses an area of 2.6 N-m = 2.6 J. Since the hysteresis is rate independent, the energy dissipated during one cycle of operation at all frequencies is 2.6 J.

LuGre Model

For the LuGre model (18), (19), the curve in Figure 4 for the input frequency $\omega = 0.1$ rad/s is essentially a hysteresis map. The area enclosed by this curve and thus dissipated during one cycle of operation at low frequency, is approximately 5×10^{-4} J.

Maxwell-Slip Model

Consider the Maxwell-slip model with N mass-spring elements as shown in Figure 5. Under periodic motion, the springs gain potential energy in compression and extension but do not return this energy to the system. The lost energy is therefore the energy dissipated by the friction. Provided $u_{max} > \Delta_i$ for all i, where u_{max} is the maximum value of the periodic input, the potential energy gained by the springs in one complete cycle of the periodic input is given by $E_{diss} = \sum_{i=1}^{N} k_i \Delta_i^2$. For the Maxwell slip model with ten elements considered in Figure 6(b), $E_{diss} = 2.4 \times 10^{-3}$ J, where J denotes Joule. By numerical integration, the area enclosed by the hysteresis map in Figure 6(b) is found to be approximately 2.5×10^{-3} J.

HYSTERESIS INDUCED BY DUHEM FEEDBACK

To study hysteresis induced by Duhem friction models, we consider the feedback interconnection of a single-input, single-output linear system and a Duhem hysteretic model as shown in Figure 11.

The following definition given in [32] is needed.

Definition 4

Consider the system in Figure 11 with constant u. The system is step convergent if $\lim_{t \to \infty} y(t)$ exists for all initial conditions and for all $u \in \mathbb{R}$.

Suppose the feedback system in Figure 11 is step convergent. Then it follows from Definition 4 that $\lim_{t \to \infty} y(t)$ exists for every constant u. Now, let $u : [0, \infty) \to [u_{min}, u_{max}]$ be periodic with period α, and let $u_T(t) = u(\alpha t/T)$ for all t. Now assume that, for all $x_0 \in \mathbb{R}^n$, the periodic input-output map $\mathcal{H}_T(u_T, y_T, x_0)$ exists for all $T > 0$ and that the limiting periodic input-output map
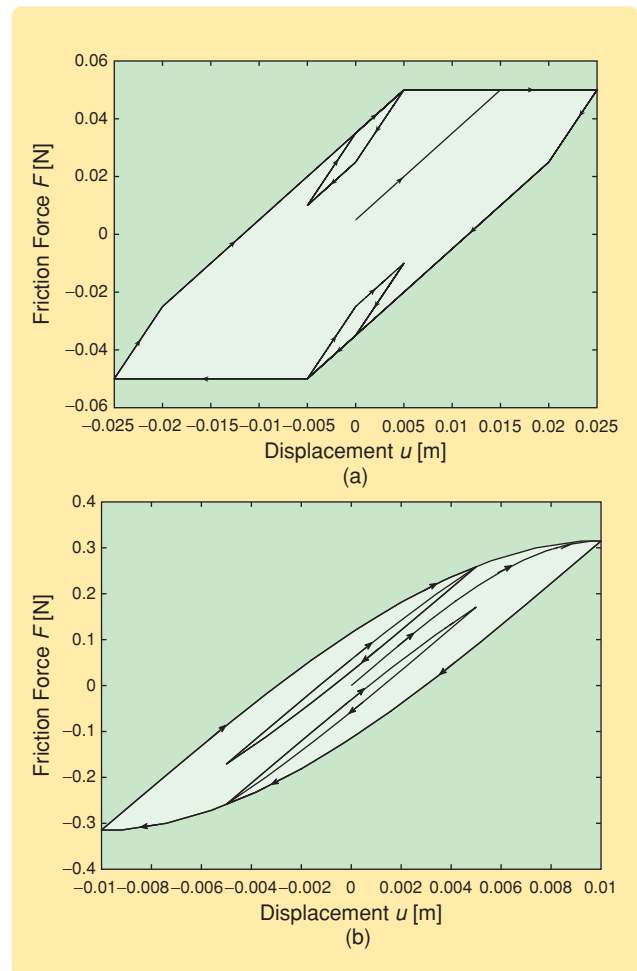

FIGURE 7 Nonlocal memory of the Maxwell-slip model with (a) $N = 2$, $\Delta_1 = 2.5 \times 10^{-3}$ m, $\Delta_2 = 1.5 \times 10^{-2}$ m, $k_1 = 2$ N/m, and $k_2 = 3$ N/m, and (b) with $N = 10$, $\Delta = [1.5, 2.4, 3.3, 4.2, 5.1, 6, 6.9, 7.8, 8.7, 9.6] \times 10^{-3}$ m, and $k = [1, 1.8, 2.6, 3.4, 4.2, 5, 5.8, 6.6, 7.4, 8.2]$ N/m. The input $u(t)$ is initially $u_1(t) = 0.025 \sin(0.1t)$ m in (a) and $u_1(t) = 0.01 \sin(0.1t)$ m in (b), where the friction force corresponds to the major loops. When $u(t)$ changes to $u_2(t) = 0.005 \sin(0.1t)$ m after one period, the friction force F corresponds to the upper minor loops. When $u(t)$ changes to $u_2(t)$ after one and a half periods, the friction force F corresponds to the lower minor loops.

$\mathcal{H}_\infty(u, x_0)$ exists. Since the set $\mathcal{H}_\infty(u, x_0)$ represents the response of the feedback system in the limit of dc operation, each element (u, y) of $\mathcal{H}_\infty(u, x_0)$ is the limit of a sequence of points $\{(u_i, y_i)\}_{i=1}^\infty$, where $(u_i, y_i) \in \mathcal{H}_{T_i}(u_{T_i}, y_{T_i}, x_0)$, as $T_i \to \infty$, that is, as the input becomes increasingly slower. Since a constant input u_∞ can be viewed as a periodic input with infinite period, the component y_∞ of each limiting point $(u_\infty, y_\infty) \in \mathcal{H}_\infty(u, x_0)$ is given by $y_\infty = \lim_{t\to\infty} y(t)$ under the constant input u_∞. This observation suggests that step convergence of the feedback system is necessary and sufficient for the existence of $\mathcal{H}_\infty(u, x_0)$.

Let $\bar{y}_1$ and $\bar{z}_1$ represent limiting values of the outputs of the linear system $G(s)$ and the Duhem model, respectively, for a constant input u. If $G(s)$ has no poles in the closed right-half plane and the system in Figure 11 is step convergent, then

$$\bar{y}_1 = G(0)(u - \bar{z}_1). \tag{27}$$

Now suppose that, for some constant u, the hysteretic Duhem model has distinct equilibria $\bar{z}_1$ and $\bar{z}_2$. Then the output of the feedback system also has distinct equilibria $\bar{y}_1 = G(0)(u - \bar{z}_1)$ and $\bar{y}_2 = G(0)(u - \bar{z}_2)$. Hence, the limiting periodic map $\mathcal{H}_\infty(u, x_0)$ exists, that is, there exists hysteresis between $u(t)$ and $y(t)$. Furthermore, for a given u, the horizontal width of the hysteresis map is given by $\bar{y}_1 - \bar{y}_2 = G(0)(\bar{z}_2 - \bar{z}_1)$. In the following section we illustrate these observations with an example.

HYSTERESIS INDUCED BY FRICTION IN A MASS-SPRING SYSTEM

We now consider the force-actuated mass-spring system shown in Figure 12, whose dynamics are given by
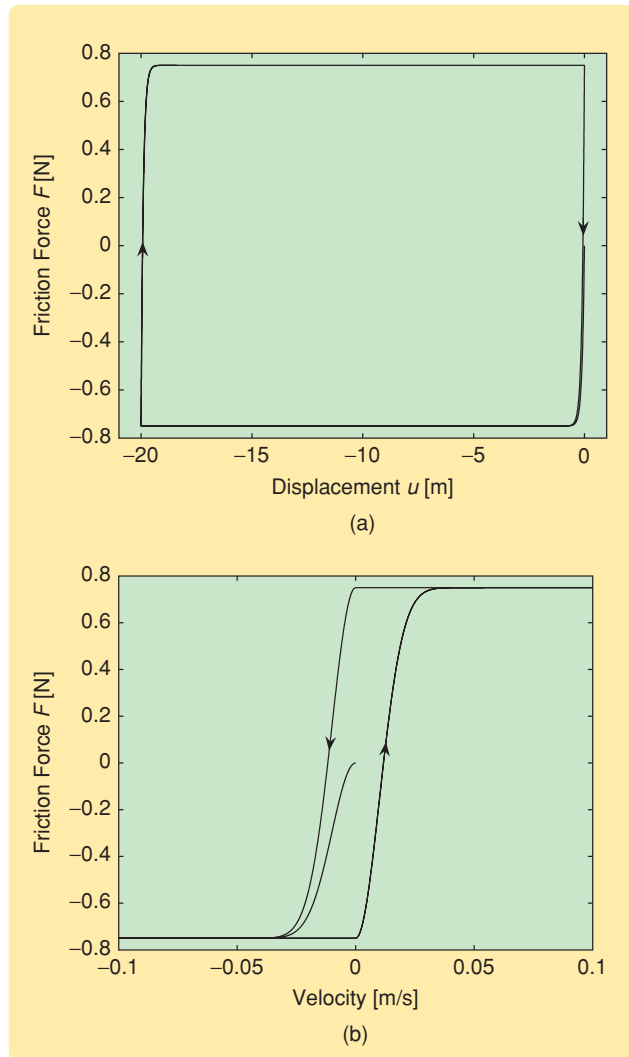

FIGURE 8 (a) Friction force versus displacement and the corresponding (b) friction force versus velocity for the Dahl model with $F_C = 0.75$ N, $\gamma = 1$, $\sigma = 7.5$ N/m, and $u(t) = 10((\cos 0.01t) - 1)$ m. The friction force saturates at F_C, while its sign reversal lags the sign change in velocity.
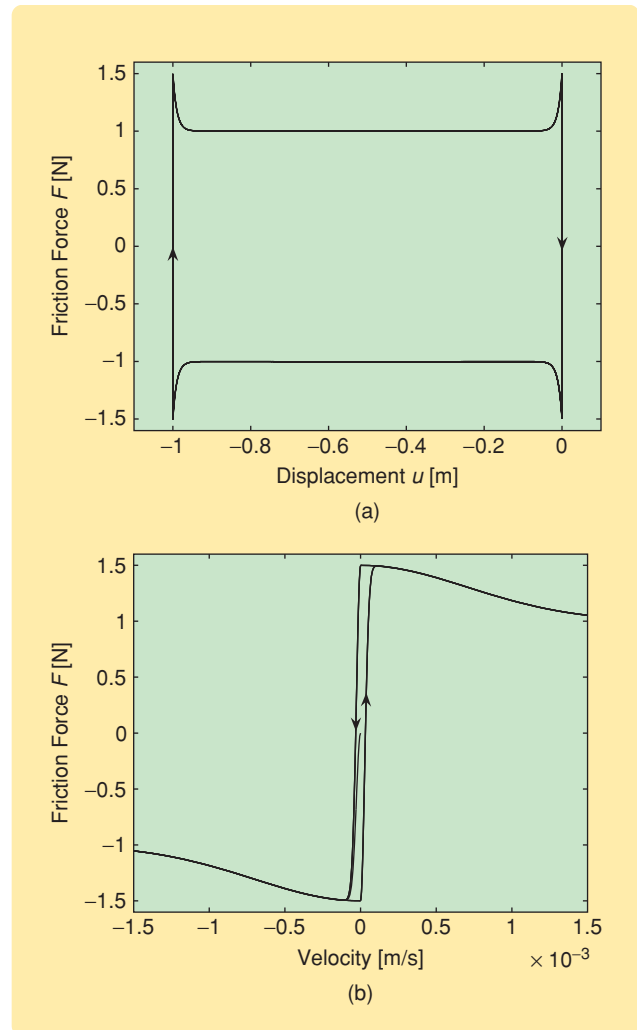

FIGURE 9 (a) Friction force versus displacement and the corresponding (b) friction force versus velocity for the LuGre model (18), (19) with $F_C = 1$ N, $F_S = 1.5$ N, $v_S = 0.001$ m/s, $\sigma_0 = 10^5$ N/m, $\sigma_1 = \sqrt{10^5}$ N-s/m, $\sigma_2 = 0.4$ N-s/m, and $u(t) = 0.01((\cos 0.01t) - 1)$ m. The friction force saturates at F_S, while its sign reversal lags the sign change in velocity.

$$\ddot{q}(t) + \frac{k_s}{m} q(t) = \frac{1}{m} F_e(t) - \frac{1}{m} F, \qquad (28)$$

where $q(t)$ is the displacement of the mass, k_s is the spring constant, m is the mass, $F_e(t)$ is the external force exerted on the mass, and F is the friction force acting on the mass. Let $v = \dot{q}$ denote the velocity of the mass.

In Figure 11, this system is represented as the feedback interconnection of a linear system with a Duhem hysteretic model, where $u = F_e$, $y = q$, $z = F$, and the transfer function $G(s)$ is given by
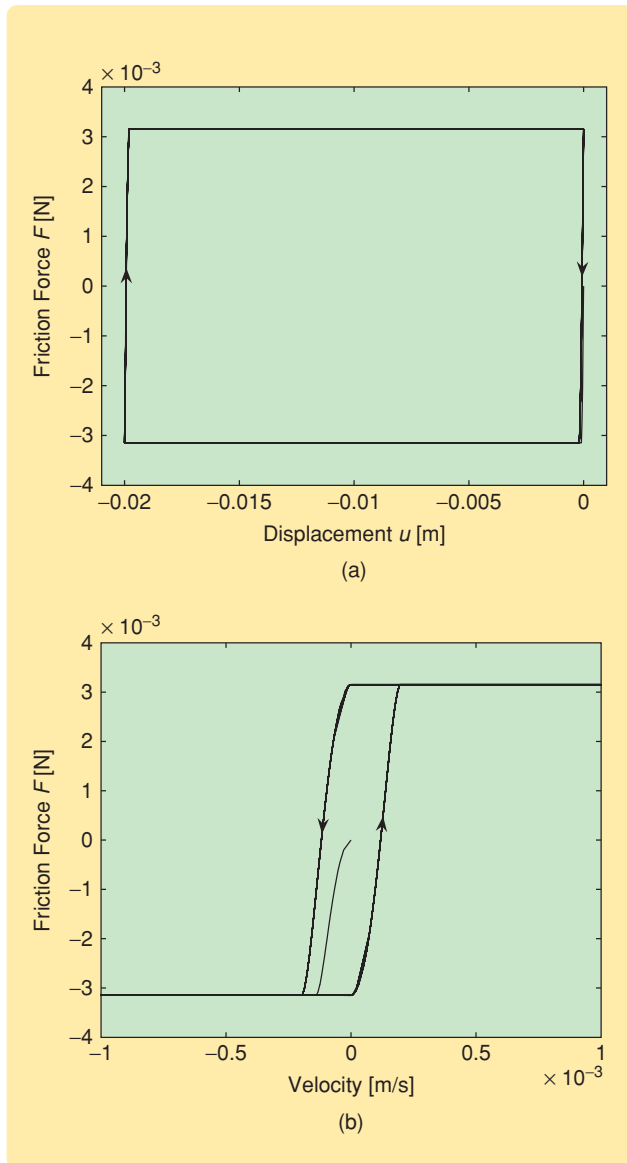

(a)

(b)

FIGURE 10 (a) Friction force versus displacement and the corresponding (b) friction force versus velocity for the Maxwell-slip model with $N = 10$, $\Delta = [1.5, 2.4, 3.3, 4.2, 5.1, 6, 6.9, 7.8, 8.7, 9.6] \times 10^{-5}$ m, $k = [1, 1.8, 2.6, 3.4, 4.2, 5, 5.8, 6.6, 7.4, 8.2]$ N/m, and $u(t) = 0.01((\cos 0.01t) - 1)$ m. The friction force sign reversal lags the sign change in velocity.

$$G(s) = \frac{1}{ms^2 + k_s}. \qquad (29)$$

Dahl Model

Using the Dahl model (11) for the friction force with mass displacement $u = q$, we have

$$\dot{F}(t) = \sigma \left| 1 - \frac{F(t)}{F_C} \operatorname{sgn} \dot{q}(t) \right|^\gamma \operatorname{sgn}\left(1 - \frac{F(t)}{F_C} \operatorname{sgn} \dot{q}(t) \right) \dot{q}(t). \qquad (30)$$

As shown above, the friction force given by the Dahl model converges to the constant values F_C or $-F_C$ depending on the sign of the relative velocity and acts in a direction opposing the motion. Consequently, the Dahl friction acting on the mass in the mass-spring system plays the role of a damper. Hence, the force-actuated mass-spring system with Dahl friction is step convergent, and the states in the feedback representation (29), (30) converge to constant values for every constant $F_e \in \mathbb{R}$. Letting $\bar{q}$, $\bar{v}$, and $\bar{F}$ denote steady-state values, (27), (28), and (30) yield
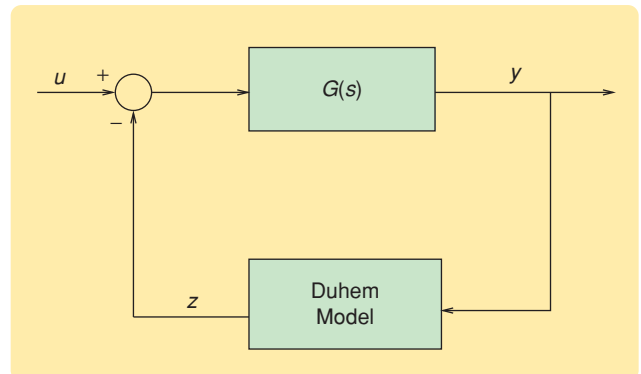

FIGURE 11 Single-input, single-output linear system with Duhem feedback. This model is used to study hysteresis induced by a Duhem friction model when connected by feedback to a linear system.
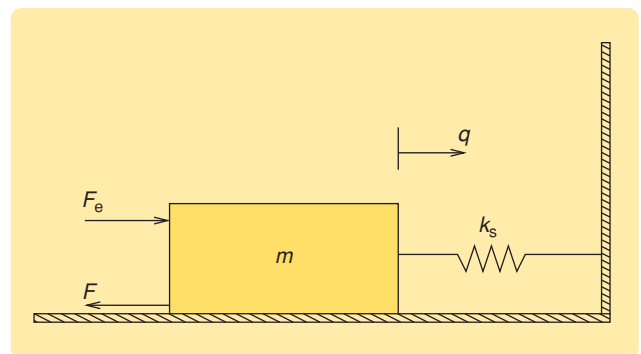

FIGURE 12 Force-actuated mass-spring system. The friction force is denoted by F, while the external force is F_e. The system exhibits hysteresis from the external force F_e to the displacement q when the Dahl and LuGre models are used to model the friction force F.

$$\bar{v} = 0, \tag{31}$$

$$\bar{q} = G(0)(u - \bar{z}) = \frac{F_e - \bar{F}}{k_s}, \tag{32}$$

$$\left(1 - \frac{\bar{F}}{F_C}\operatorname{sgn}\bar{v}\right) = 0. \tag{33}$$

For a constant external force input, the steady-state values of displacement, velocity, and friction force are given by (31), (32), and (33), respectively. Thus, for a low-frequency external force input, $v(t) \to 0$ as $t \to \infty$, and the displacement of the mass satisfies $q(t) \to \bar{q}$ as $t \to \infty$, where $\bar{q}$ is given by (32). Now, if (33) holds, then $\bar{F} = F_C$ or $\bar{F} = -F_C$ depending on the sign of $v(t)$. Consequently, from (32), the steady-state displacement $\bar{q}$ can assume two different values, namely,

$$\bar{q}_1 = G(0)(F_e + F_C) = \frac{F_e + F_C}{k_s},$$

$$\bar{q}_2 = G(0)(F_e - F_C) = \frac{F_e - F_C}{k_s}.$$

These observations suggest that the limit of the periodic map $\mathcal{H}_T(F_{eT}, q_T)$ exists as $T \to \infty$, that is, there exists hysteresis between $F_e(t)$ and $q(t)$. The width of the map is given by $\bar{q}_1 - \bar{q}_2 = 2F_c/k_s$. For $k_s = 1.5$ N/m, $F_c = 0.75$ N,

and $F_e(t) = 5\sin(0.001t)$ N, the hysteresis map from the mass displacement $q(t)$ to the external force $F_e(t)$ is shown in Figure 13. It can be seen that the vertical width of the hysteresis map is 1 m.

LuGre Model

Using the LuGre model (18), (19) with $u(t) = q(t)$, we have

$$\dot{x}(t) = \dot{q}(t) - \frac{|\dot{q}(t)|}{r(\dot{q}(t))}x(t), \tag{34}$$

$$F(t) = \sigma_0 x(t) + \sigma_1 \dot{x}(t) + \sigma_2 \dot{q}(t), \tag{35}$$

where

$$r(\dot{q}(t)) = \frac{F_C}{\sigma_0} + \frac{F_S - F_C}{\sigma_0}e^{-(\dot{q}(t)/v_S)^2}. \tag{36}$$

Due to the Stribeck effect, relating the equilibria map to the hysteresis map in the case of the LuGre model is more complicated compared to the Dahl model. The friction force acts in a direction opposing the motion and, consequently, plays the role of a damper in the force-actuated mass-spring system. Hence, the force-actuated
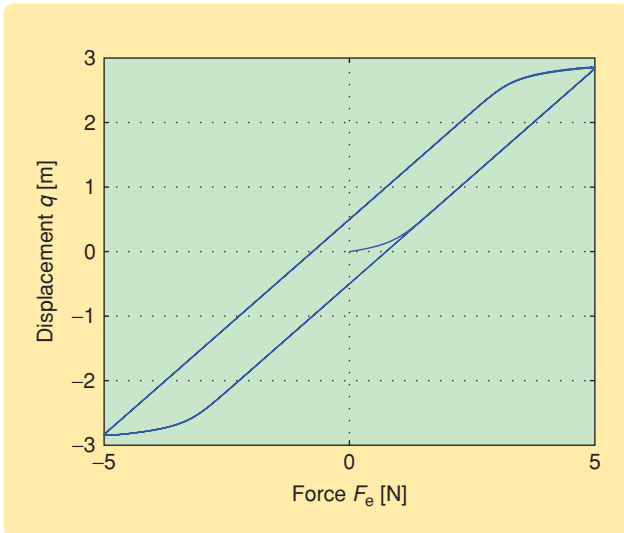

FIGURE 13 Hysteresis map from the external force $F_e(t)$ to the displacement $q(t)$ of the mass for the force-actuated mass-spring system (28) in Figure 12, with the Dahl model. The numerical values are $F_C = 0.75$ N, $\gamma = 1$, $\sigma = 7.5$ N/m, $k_s = 1.5$ N/m, $m = 1$ kg, and $F_e(t) = 5\sin(0.001t)$ N. The vertical width of the hysteresis map is 1 m.
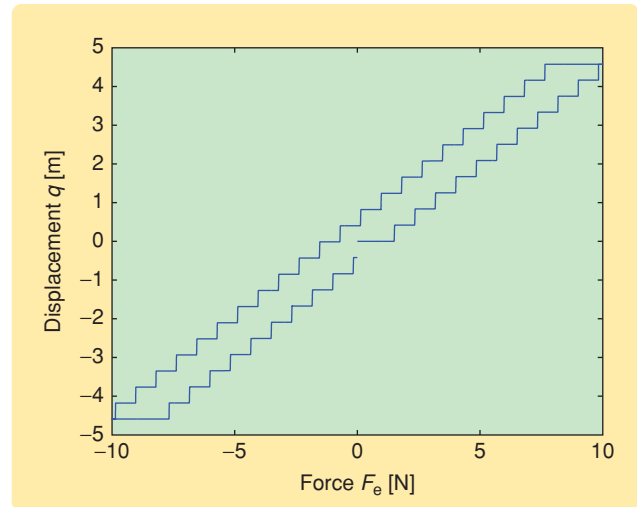

FIGURE 14 Hysteresis map from the external force $F_e(t)$ to the displacement $q(t)$ of the mass for the force-actuated mass-spring system (28) in Figure 12, with the LuGre model (34), (35). The staircase pattern is caused by the Stribeck effect in the LuGre model. The numerical values are $F_C = 1$ N, $F_S = 1.5$ N, $v_S = 0.001$ m/s, $\sigma_0 = 10^5$ N/m, $\sigma_1 = \sqrt{10^5}$ N-s/m, $\sigma_2 = 0.4$ N-s/m, and $F_e(t) = 10\sin(0.001t)$ N.

mass-spring system with LuGre friction is step convergent, and the states in the feedback representation given by (29), (34), and (35) converge to constant values for every constant $F_e \in \mathbb{R}$.

The hysteresis map from the input F_e to the output q for a low-frequency input $F_e = 10\sin(0.001t)$ N is shown in Figure 14. The time histories of the friction force F and the position of the mass q are shown in Figure 15. The mass-spring system exhibits stick-slip motion [10] in which the mass sticks until the friction force exceeds the breakaway force F_S. Once the mass starts moving, the friction force drops because of the Stribeck effect. Consequently, the mass accelerates, and thus the spring contracts and the spring force increases. The mass accelerates until the external force is balanced by the friction force and the spring force. When the spring force becomes sufficiently large, the mass decelerates and sticks again. This process repeats. Stick-slip is reflected by the regions of zero velocity shown in Figure 15(b). The staircase pattern in the hysteresis map shown in Figure 14 is caused by the stick-slip motion. The low-slope horizontal segments of the map correspond to sticking, while the high-slope vertical segments correspond to slip. It should be noted that the hysteresis map is continuous despite the steep vertical segments.

The amplitude of the oscillations in the friction force shown in Figure 15(a) is equal to $F_S - F_C = 0.5$ N. The length ΔF_e of the horizontal segments of the hysteresis map is twice the amplitude of the oscillations in the friction force, that is, $\Delta F_e = 1$ N. The horizontal segments correspond to the sticking phase of the motion, in which the mass is at rest and thus the external force is balanced by the spring force and the friction force. As the external force increases, the friction force also increases until reaching F_S, after which the mass slips, the friction force drops, and the spring force increases. The larger spring force causes the mass to stick again, leading to new balanced forces.

The vertical segments of the hysteresis map correspond to the slipping phase, and their size can be determined by balancing forces. For instance, consider the first vertical step starting from the origin in the hysteresis map in Figure 15(b). Let Δq denote the length of the vertical segment. The external force is $F_e = 1.5$ N, and it can be seen in Figure 15(a) that the friction force drops to $F = 0.6$ N. By balancing the forces, we have thus the spring force

$$k_s \Delta q = F_e - F = 1.5 - 0.6 = 0.9 \ \text{N},$$
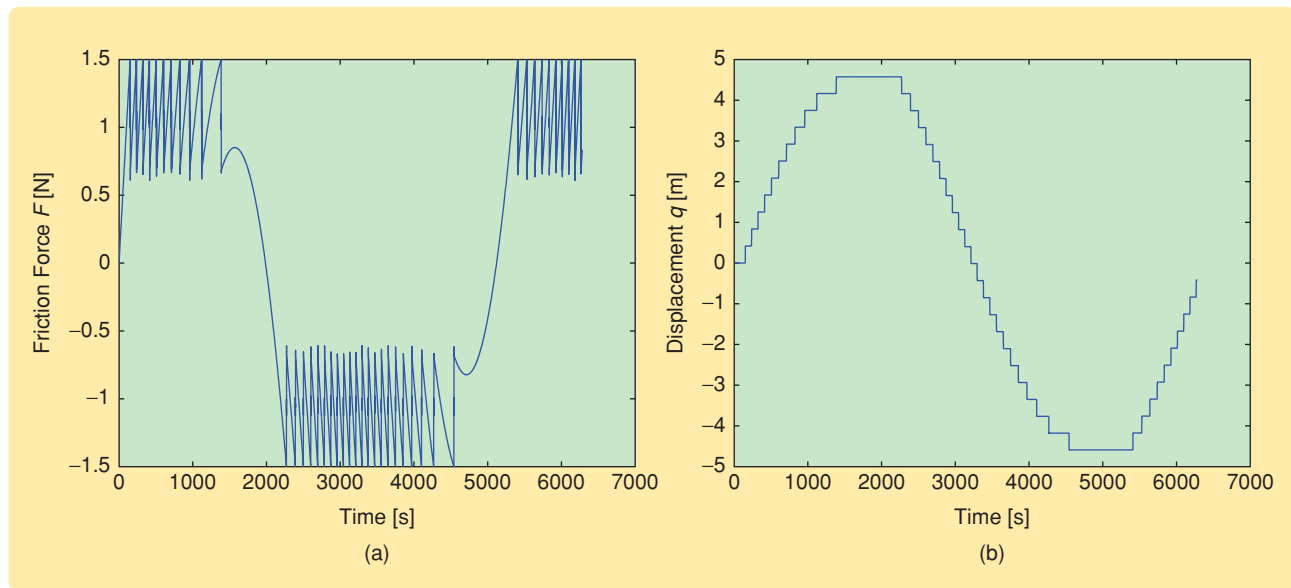
which implies that

FIGURE 15 (a) Friction force $F(t)$ and (b) displacement $q(t)$ of the mass for the force-actuated mass-spring system (28) in Figure 12, with the LuGre model (34), (35). The friction force oscillates with amplitude $F_S - F_C$, and the mass exhibits stick-slip motion. The numerical values are $F_C = 1$ N, $F_S = 1.5$ N, $v_S = 0.001$ m/s, $\sigma_0 = 10^5$ N/m, $\sigma_1 = \sqrt{10^5}$ N-s/m, $\sigma_2 = 0.4$ N-s/m, and $F_e(t) = 10\sin(0.001t)$ N.

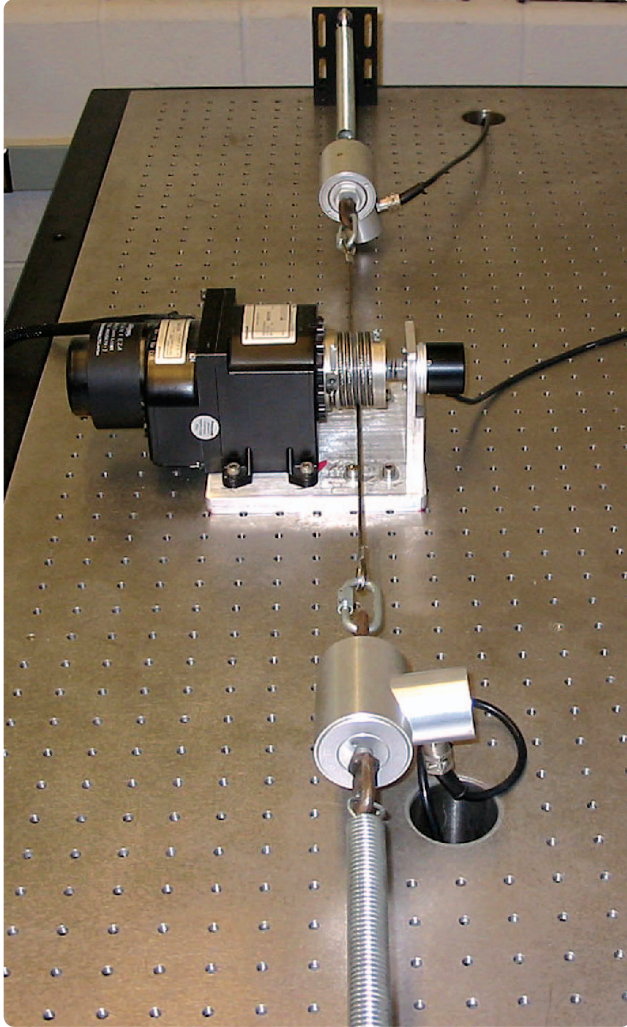$$\Delta q = \frac{0.9}{k_s} = \frac{0.9}{2} \ \text{m} = 0.45 \ \text{m}.$$

FIGURE 16 Experimental setup. This testbed involves a dc motor with a gearbox for studying the effects of gearbox friction. A pair of cables are wound around a drum attached to the gearbox and connected to a pair of springs through two load cells. The forces exerted by the springs are measured by the load cells.
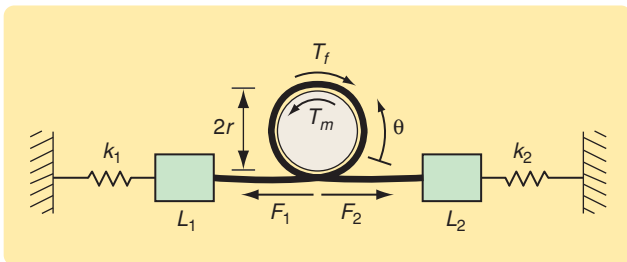

FIGURE 17 Schematic of the experimental setup looking toward the drum along its axis. The motor is behind the drum and is not shown. The drum angle θ is positive for counterclockwise rotation of the shaft.

The hysteresis map can thus be completely determined in terms of the parameters F_S, F_C, m, and k_s.

EXPERIMENTAL SETUP

We now describe an experimental setup for studying the effects of gearbox friction on the dynamics of a dc motor. The experimental setup is shown in Figure 16, while a schematic of the setup is shown in Figure 17. Two cables are wound around a drum attached to the motor shaft and connected to load cells L_1 and L_2, which measure the force exerted by the springs k_1 and k_2. Since hysteresis is an asymptotically low-frequency phenomenon, the inertia of the load cells does not affect the hysteretic properties of the system.

The dynamics of the drum are given by

$$I\ddot{\theta} = T_m - T_f + F_2 r - F_1 r, \tag{37}$$

where θ is the angle of rotation of the drum, I is the drum's moment of inertia, T_m is the torque exerted by the motor, T_f is the torque due to friction, r is the radius of the drum, and F_1 and F_2 are the forces exerted on the drum by the springs. The cables are wound such that, as the shaft rotates counterclockwise, F_1 increases and F_2 decreases. The springs are sufficiently pre-stressed that neither spring slacks while the shaft rotates in either direction. Let F_{10} and F_{20} denote the values of the spring forces at the initial drum angle, and let δ_1 and δ_2 denote the deflections in the two springs. Then

$$F_1 = F_{10} + k_1\delta_1, \quad F_2 = F_{20} + k_2\delta_2$$

and

$$\delta_1 = r\theta, \quad \delta_2 = -r\theta.$$

Hence,

$$I\ddot{\theta} = T_m - T_f - (F_{10} - F_{20})r - (k_1 + k_2)r^2\theta. \tag{38}$$

The motor torque T_m is assumed to be proportional to the motor current, that is,

$$T_m = k_m i_m, \tag{39}$$

where k_m is the proportionality constant and i_m is the motor current. Hence, (38) becomes

$$\ddot{\theta}(t) + \frac{(k_1 + k_2)r^2}{I}\theta(t) = \frac{k_m}{I}i_m(t) - \frac{1}{I}T_f - \frac{(F_{10} - F_{20})r}{I}. \tag{40}$$

If $F_{10} = F_{20}$, then, with the correspondences

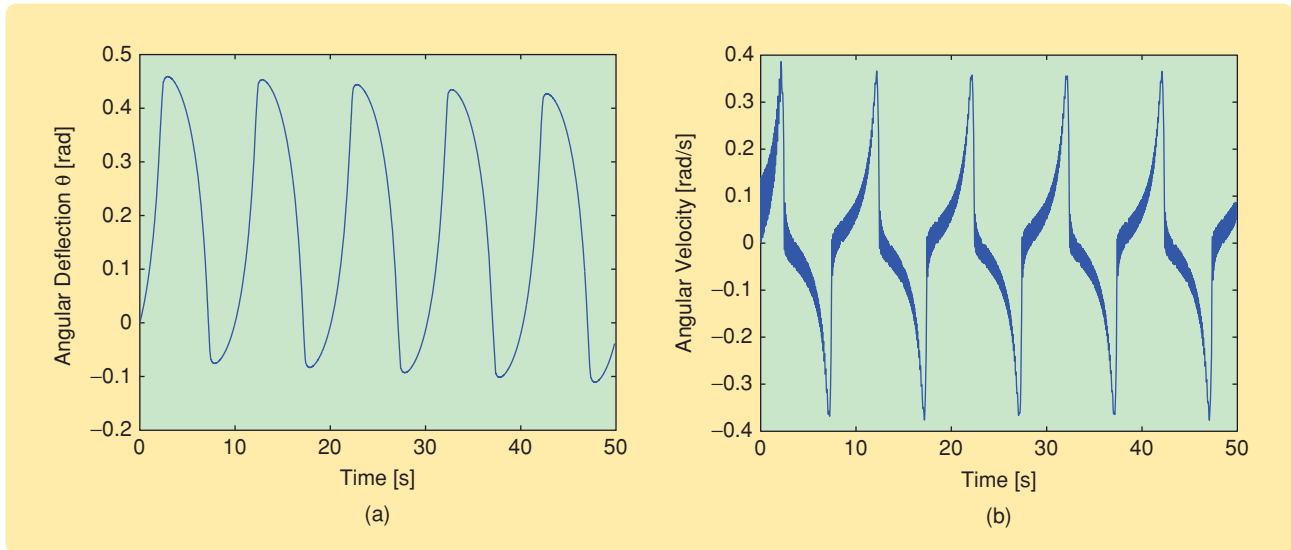**FIGURE 18** Simulation of the experimental setup with the Dahl model. (a) Drum angle θ and (b) drum angular velocity $\dot{\theta}$. The numerical values are $F_C = 0.84$ N-m, $\gamma = 1$, $\sigma = 7.5$ N-m/rad, and $i_m(t) = 0.05 \sin(0.2\pi t)$ A.

$$\frac{k_s}{m} = \frac{(k_1 + k_2)r^2}{I},$$
$$\frac{F_e}{m} = \frac{k_m}{I} i_m,$$
$$\frac{F}{m} = \frac{1}{I} T_f, \tag{41}$$

the dynamics in (40) are identical to the dynamics of the mass-spring system (28).

The setup is connected to a digital computer through a dSPACE 1103 system, which has one encoder, five analog to digital (A/D) channels, and five digital to analog (D/A) channels. Each load cell, whose output is amplified by an Endevco voltage amplifier model 136, can measure a maximum load of 75 kg and has a sensitivity of 0.26 mV/kg. The amplifier gain can be set between zero and 1000, and the amplified signals are sampled by the dSPACE system. The dc motor has a built-in tachometer that measures the angular velocity of the motor shaft. The angular velocity signal is read through an A/D channel. The conversion for the tachometer output is 0.01 V/rpm. A Heidenhain encoder measures the angle of the drum. The gear ratio between the motor shaft and the drum is 1:68.8. Current is supplied to the dc motor through a Quanser linear current amplifier LCAM. The required current profile is commanded to the current amplifier through one of the D/A channels. The

amplifier provides a voltage signal proportional to the current supplied to the dc motor. Estimated parameter values are $k_1 = k_2 = 2$ N/m, $F_{10} = F_{20} = 0.01$ N, $r = 1$ inch, $k_m = 16.5$ N-m/A, and $I = 3 \times 10^{-4}$ kg-m^2.
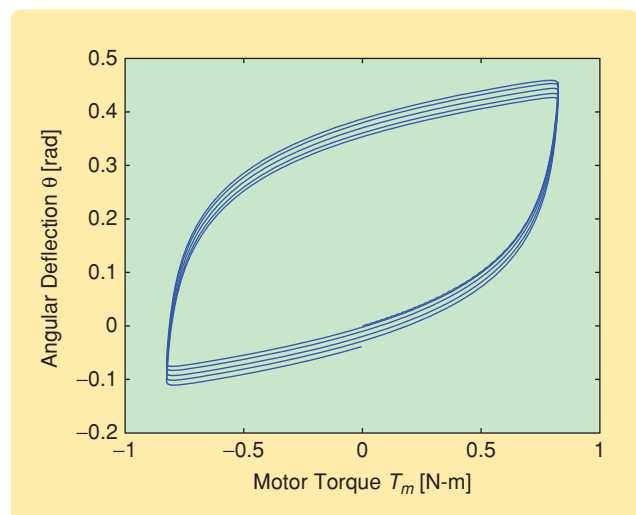

FIGURE 19 Simulation of hysteresis in the experimental setup with the Dahl model. The hysteresis map is from the motor torque T_m to the drum angle θ. The numerical values are $F_C = 0.84$ N-m, $\gamma = 1$, $\sigma = 7.5$ N-m/rad, and $i_m(t) = 0.05 \sin(0.2\pi t)$ A.
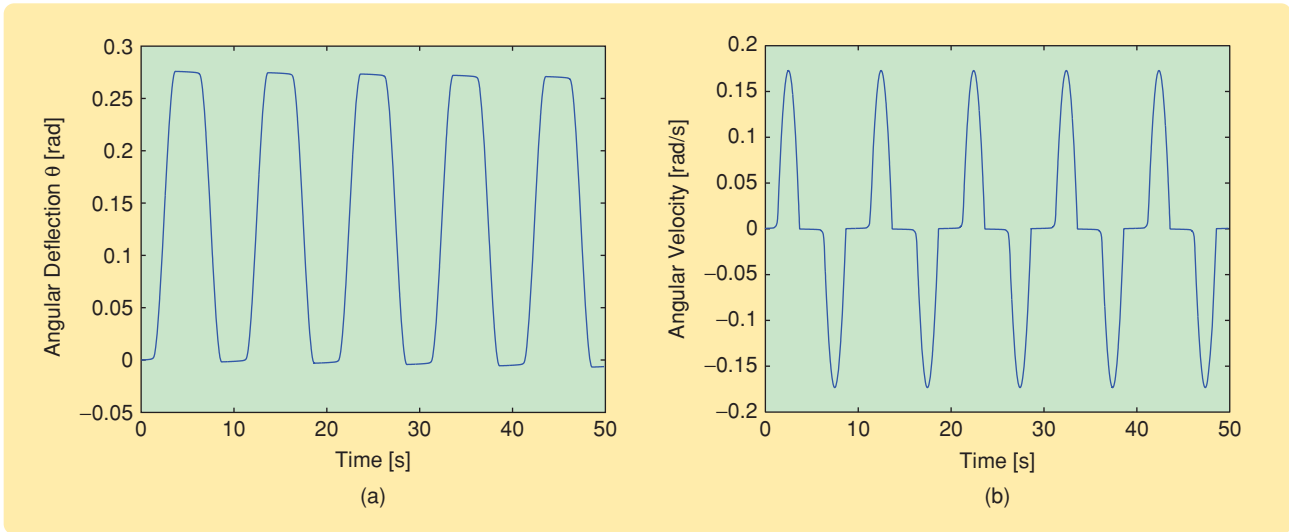
FIGURE 20 Simulation of the experimental setup with the LuGre friction model showing (a) drum angle θ and (b) drum angular velocity. The numerical values are $F_C = 0.6$ N-m, $F_S = 1$ N-m, $v_S = 0.001$ rad/s, $\sigma_0 = 10^3$ N-m/rad, $\sigma_1 = \sqrt{10^3}$ N-m-s/rad, $\sigma_2 = 1.3$ N-m-s/rad, and $i_m(t) = 0.05\sin(0.2\pi t)$ A.

SIMULATION RESULTS

In this section we simulate the dc motor dynamics (40). The friction torque T_f is modeled using the Dahl, LuGre, and Maxwell-slip models. The motor current is chosen to be $i_m(t) = 0.05\sin(0.2\pi t)$ A. For the Dahl model, the drum angle θ and the drum angular velocity $\dot{\theta}$ are shown in Figure 18. The hysteresis map from the motor torque T_m to the drum angle θ is shown in Figure 19. For the LuGre model, θ and $\dot{\theta}$ are shown in Figure 20, while the hysteresis map from the motor torque to the drum angle θ is shown in Figure 21. For the Maxwell-slip model, θ and $\dot{\theta}$ are shown in Figure 22, while the hysteresis map from the motor torque to the drum angle θ is shown in Figure 23.
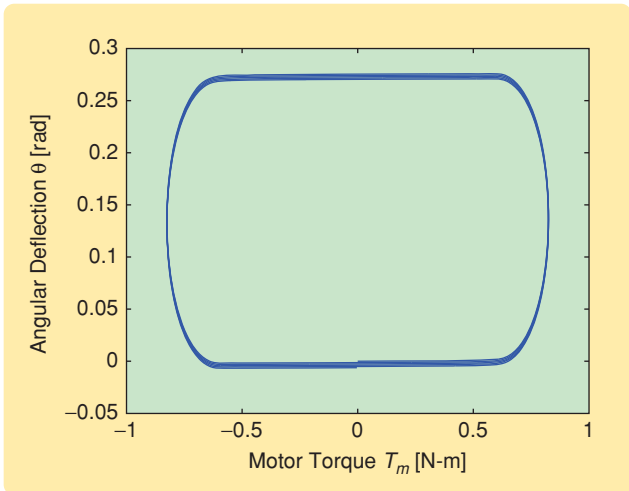

FIGURE 21 Simulation of hysteresis in the experimental setup with the LuGre model. The hysteresis map is from the motor torque T_m to the drum angle θ. The numerical values are $F_C = 0.6$ N-m, $F_S = 1$ N-m, $v_S = 0.001$ rad/s, $\sigma_0 = 10^3$ N-m/rad, $\sigma_1 = \sqrt{10^3}$ N-m-s/rad, $\sigma_2 = 1.3$ N-m-s/rad, and $i_m(t) = 0.05\sin(0.2\pi t)$ A.
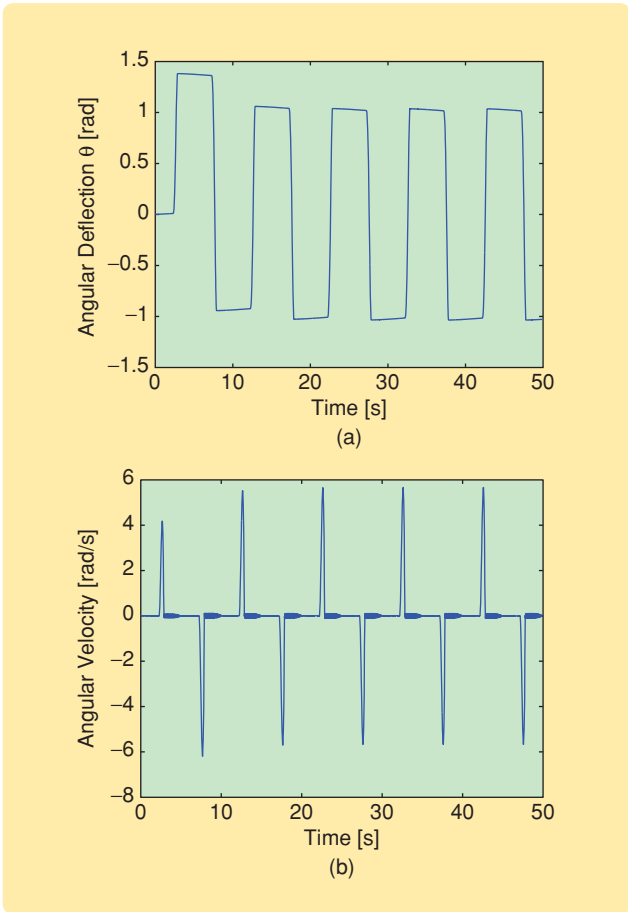

FIGURE 22 Simulation of the experimental setup with the Maxwell-slip model. (a) Angular deflection θ and (b) angular velocity $\dot{\theta}$ of the motor shaft. The numerical values are $N = 10$, $\Delta = [1.5, 2.4, 3.3, 4.2, 5.1, 6, 6.9, 7.8, 8.7, 9.6] \times 10^{-3}$ rad, $k = [2.60, 4.68, 6.76, 8.84, 10.92, 13.00, 15.08, 17.16, 19.24, 21.32]$ N-m/rad, and $i_m = 0.05\sin(0.2\pi t)$ A.

EXPERIMENTAL RESULTS

In this section we present and analyze results obtained from the experimental setup. The current profile commanded to the current amplifier is $0.05\sin(0.2\pi t)$ A. The load cell readings, the actual current supplied by the amplifier to the dc motor, the shaft angular velocity measured by the tachometer, and the drum angle measured by the encoder are shown in Figure 24. Because of asymmetry in the setup, the force values F_{10} and F_{20} in the two springs are not equal. Once the current supply is switched on, the motor shaft reaches an equilibrium position at approximately $t = 5$ s in which both springs are equally stressed and then oscillates about that position. This behavior is evident in the load cell readings as shown in Figure 24.

The motor shaft rotates slowly in one direction until the motor torque cannot exceed the torque exerted by the springs and the gearbox friction, after which the motor stops rotating and remains motionless until the motor torque changes direction. This behavior can be seen in Figure 24 where the shaft has zero angular velocity in periodic time intervals, which matches best with the angular velocity obtained from the simulations using the LuGre model shown in Figure 20(b). The motor torque and drum angle exhibiting hysteresis in the experiment are shown in Figure 25. After initial transients, the motion approaches a hysteresis map.

Aside from the transients and the bias in the motor torque, the hysteresis map in Figure 25 has the same form as the map simulated using the LuGre model shown in Figure 21. Consequently, of the three friction models considered, the LuGre model provides the best model of the gearbox friction.

Parameter Identification

Since simulation with the LuGre model gives a hysteresis map that qualitatively resembles the experimental hysteresis map, we determine LuGre friction parameters to quantitatively match the simulated and experimental hysteresis maps. Using a manual tuning approach, suitable parameter values are found to be $F_C = 0.6$ N-m, $F_S = 1$ N-m, $v_S = 0.001$ rad/s, $\sigma_0 = 10^3$ N-m/rad, $\sigma_1 = \sqrt{10^3}$ N-m-s/rad, and $\sigma_2 = 1.3$ N-m-s/rad. Simulation of the experimental setup using these parameters yields the plots of θ and $\dot\theta$ shown in Figure 20. Figure 26 compares the experimental and simulated hysteresis maps. Adjustments are made for bias in the motor current and asymmetry in the motor setup.
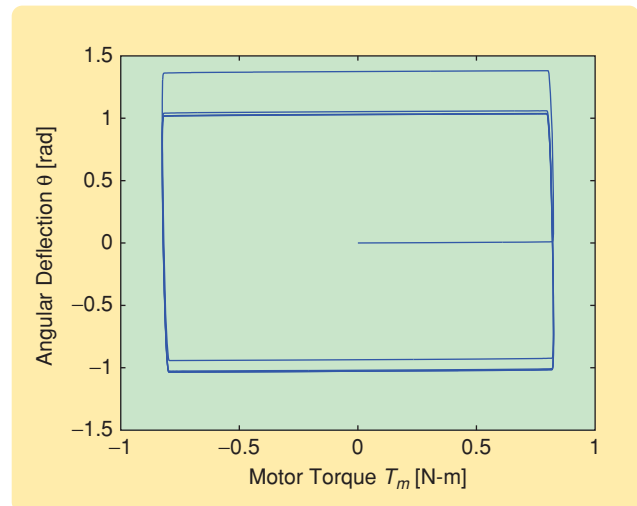

FIGURE 23 Simulation of hysteresis in the experimental setup with the Maxwell-slip model. This hysteresis map is from the motor torque T_m to the drum angle θ. The numerical values are $N = 10$, $\Delta = [1.5, 2.4, 3.3, 4.2, 5.1, 6, 6.9, 7.8, 8.7, 9.6] \times 10^{-3}$ rad, $k = [2.60, 4.68, 6.76, 8.84, 10.92, 13.00, 15.08, 17.16, 19.24, 21.32]$ N-m/rad, and $i_m = 0.05\sin(0.2\pi t)$ A.
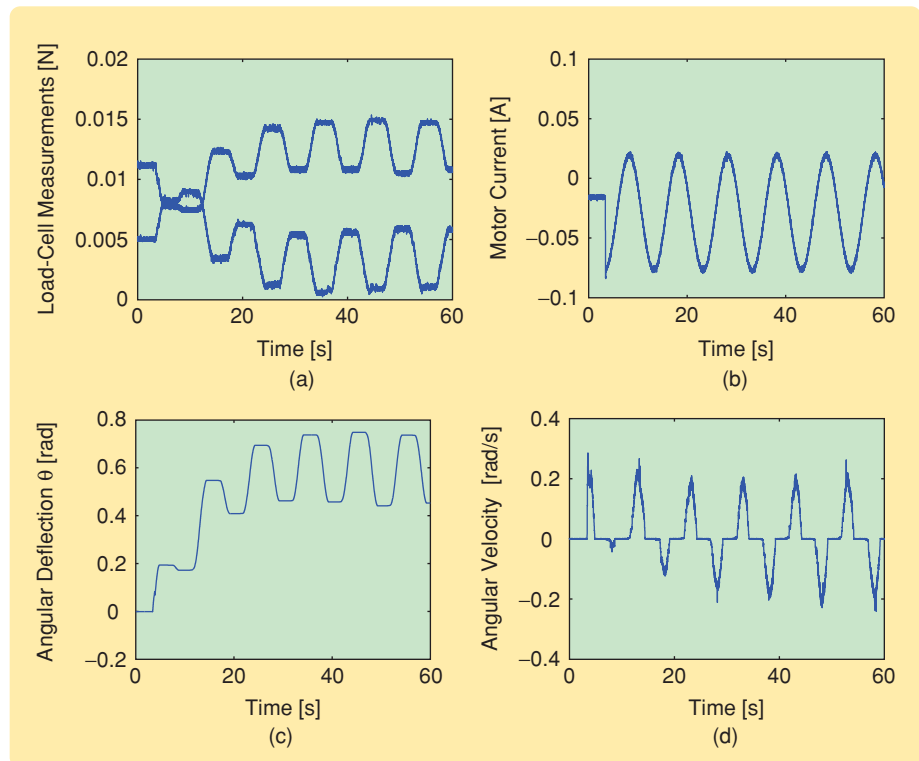

FIGURE 24 Experimental results. These plots show (a) load-cell measurements, (b) current supplied by the amplifier, (c) the drum angle, and (d) the drum angular velocity readings for the dc motor experiment. The input current is $i_m(t) = 0.05\sin(0.2\pi t)$ A. Note that the drum angular velocity plot resembles the plot in Figure 20(b).

> **By comparing the simulated and experimental results, it was found that the LuGre model provides the best model of the gearbox friction characteristics.**
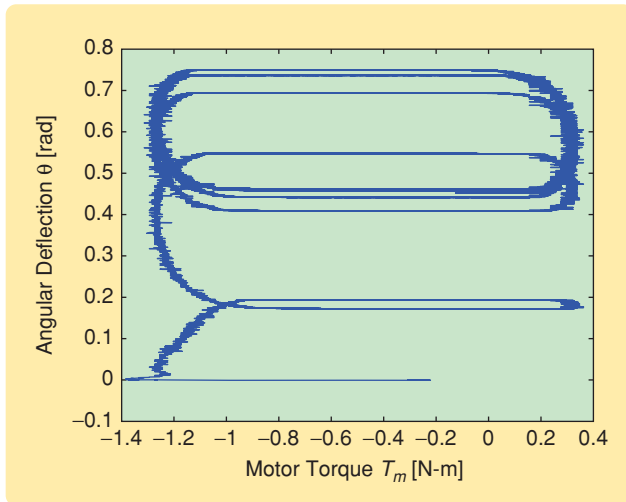

FIGURE 25 Hysteresis in the dc motor experiment from the motor torque to the drum angle. The input current is $i_m(t) = 0.05\sin(0.2\pi t)$ A. Aside from the transients and the bias in the motor torque, the hysteresis map is similar in form to the simulated hysteresis map in Figure 21, based on the LuGre model.
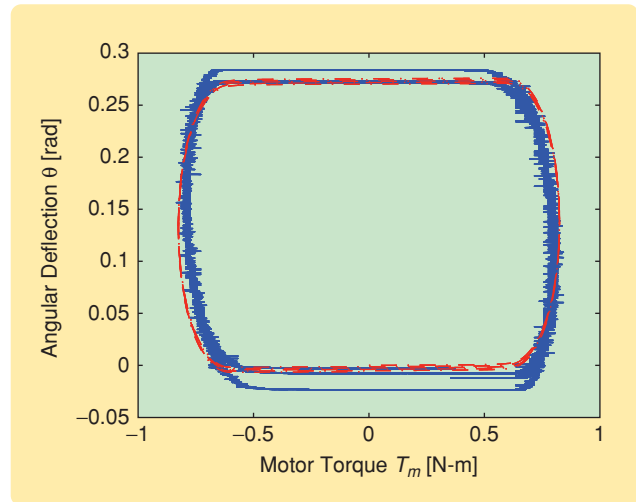

FIGURE 26 Matching the experimental hysteresis map and the simulated hysteresis map based on the LuGre model. The hysteresis map is from the motor torque T_m to the drum angle θ. The numerical values for the simulations are $F_C = 0.6$ N-m, $F_S = 1$ N-m, $v_S = 0.001$ rad/s, $\sigma_0 = 10^3$ N-m/rad, $\sigma_1 = \sqrt{10^3}$ N-m-s/rad, and $\sigma_2 = 1.3$ N-m-s/rad. The input current is $i_m(t) = 0.05\sin(0.2\pi t)$ A for both the experiment and the simulation.

CONCLUSIONS

In this article we recast the Dahl, LuGre, and Maxwell-slip models as extended, generalized, or semilinear Duhem models. We classified each model as either rate independent or rate dependent. Smoothness properties of the three friction models were also considered.

We then studied the hysteresis induced by friction in a single-degree-of-freedom system. The resulting system was modeled as a linear system with Duhem feedback. For each friction model, we computed the corresponding hysteresis map. Next, we developed a dc servo motor testbed and performed motion experiments. We then modeled the testbed dynamics and simulated the system using all three friction models. By comparing the simulated and experimental results, it was found that the LuGre model provides the best model of the gearbox friction characteristics. A manual tuning approach was used to determine parameters that model the friction in the dc motor.

ACKNOWLEDGMENTS

REFERENCES

[1] B. Armstrong-Hélouvry, *Control of Machines with Friction*. Boston, MA: Kluwer, 1991.

[2] B. Armstrong-Hélouvry, P. Dupont, and C. Canudas de Wit, "A survey of model, analysis tools and compensation methods for the control of machines with friction," *Automatica*, vol. 30, no. 7, pp. 1083–1138, 1994.

[3] B. Feeny, A. Guran, N. Hinrichs, and K. Popp, "Historical review on dry friction and stick-slip phenomena," *Appl. Mech. Rev.*, vol. 51, no. 5, pp. 321–341, 1998.

[4] M.A. Krasnoselskii and A.V. Pokrovskii, *Systems with Hysteresis*. New York: Springer-Verlag, 1980.

[5] J.W. Macki, P. Nistri, and P. Zecca, "Mathematical models for hysteresis," *SIAM Rev.*, vol. 35, no. 1, pp. 94–123, 1993.

[6] P. Dahl, "Solid friction damping of mechanical vibrations," *AIAA J.*, vol. 14, no. 2, pp. 1675–1682, 1976.

[7] D.D. Rizos and S.D. Fassois, "Presliding friction identification based upon the Maxwell slip model structure," *Chaos*, vol. 14, no. 2, pp. 431–445, 2004.

[8] F. Al-Bender, V. Lampaert, and J. Swevers, "The generalized Maxwell-slip model: A novel model for friction simulation and compensation," *IEEE Trans. Autom. Contr.*, vol. 50, no. 11, pp. 1883–1887, 2005.

[9] V. Lampaert, J. Swevers, and F. Al-Bender, "Modification of the Leuven integrated friction model structure," *IEEE Trans. Autom. Contr.*, vol. 47, no. 4, pp. 683–687, 2002.

[10] C. Canudas de Wit, H. Olsson, K.J. Åstrom, and P. Lischinsky, "A new model for control of systems with friction," *IEEE Trans. Autom. Contr.*, vol. 40, no. 3, pp. 419–425, 1995.

[11] J. Swevers, F. Al-Bender, C.G. Ganseman, and T. Prajogo, "An integrated friction model structure with improved presliding behavior for accurate friction compensation," *IEEE Trans. Autom. Contr.*, vol. 45, no. 4, pp. 675–686, 2000.

[12] F. Al-Bender, V. Lampaert, and J. Swevers, "Modeling of dry sliding friction dynamics: From heuristic models to physically motivated models and back," *Chaos*, vol. 14, no. 2, pp. 446–445, 2004.

[13] F. Al-Bender, V. Lampaert, S.D. Fassois, D.D. Rizos, K. Worden, D. Engster, A. Hornstein, and U. Parlitz, "Measurement and identification of pre-sliding friction dynamics," in *Nonlinear Dynamics of Production Systems,* G. Radons and R. Neugebauer, Eds. Weinheim: Wiley, 2004, pp. 349–367.

[14] G. Ferretti, G. Magnani, and P. Rocco, "Single and multistate integral friction models," *IEEE Trans. Autom. Contr.*, vol. 49, no. 12, pp. 2292–2297, 2004.

[15] J. Amin, B. Friedland, and A. Harnoy, "Implementation of a friction estimation and compensation technique," *IEEE Contr. Sys. Mag.*, vol. 17, no. 4, pp. 71–76, 1997.

[16] S.C. Southward, C.J. Radcliffe, and C.R. MacCluer, "Robust nonlinear stick-slip friction compensation," *J. Dynam. Syst. Meas. Contr.*, vol. 113, no. 4, pp. 639–645, 1991.

[17] S.-W. Lee and J.-H. Kim, "Robust adaptive stick-slip friction compensation," *IEEE Trans. Ind. Electron.*, vol. 42, no. 5, pp. 474–479, 1995.

[18] R.-H. Wu and P.-C. Tung, "Studies of stick-slip friction, presliding displacement, and hunting," *J. Dynam. Syst., Meas. Contr.*, vol. 124, no. 1, pp. 111–117, 2002.

[19] M. Marques, *Differential Inclusions in Nonsmooth Mechanical Problems: Shocks and Dry Friction*. Cambridge, MA: Birkhaüser, 1993.

[20] S.P. Bhat and D.S. Bernstein, "Finite-time stability of continuous autonomous systems," *SIAM J. Contr. Optimiz.*, vol. 38, pp. 751–766, 2000.

[21] S.P. Bhat and D.S. Bernstein, "Continuous finite-time stabilization of the translational and rotational double integrators," *IEEE Trans. Autom. Contr.*, vol. 43, no. 5, pp. 678–682, 1998.

[22] J. Oh and D.S. Bernstein, "Step convergence analysis of nonlinear feedback hysteresis models," in *Proc. American Control Conf.*, Portland, OR, 2005, pp. 697–702.

[23] D. Angeli and E.D. Sontag, "Multi-stability in monotone input/output systems," *Sys. Contr. Lett.*, vol. 51, pp. 185–202, 2004.

[24] D. Angeli, J.E. Ferrell, and E.D. Sontag, "Detection of multistability, bifurcations, and hysteresis in a large class of biological positive feedback systems," in *Proc. Nat. Academy Science*, 2004, vol. 101, no. 7, pp. 1822–1827.

[25] J. Oh and D.S. Bernstein, "Semilinear Duhem model for rate-independent and rate-dependent hysteresis," *IEEE Trans. Autom. Contr.*, vol. 50, no. 5, pp. 631–645, 2005.

[26] A. Visintin, *Differential Models of Hysteresis*. New York: Springer-Verlag, 1994.

[27] P.A. Bliman, "Mathematical study of the Dahl's friction model," *Euro. J. Mech. Solids*, vol. 11, no. 6, pp. 835–848, 1992.

[28] Y.Q. Ni, Z.G. Ying, J.M. Ko, and W.Q. Zhu, "Random response of integrable Duhem hysteretic systems under non-white excitation," *Int. J. Non-Linear Mech.*, vol. 37, no. 8, pp. 1407–1419, 2002.

[29] N. Barabanov and R. Ortega, "Necessary and sufficient conditions for passivity of the LuGre friction model," *IEEE Trans. Autom. Contr.*, vol. 45, no. 4, pp. 830–832, 2000.

[30] J. Swevers, F. Al-Bender, C. Ganseman, and T. Projogo, "An integrated friction model structure with improved presliding behavior for accurate friction compensation," *IEEE Trans. Autom. Contr.*, vol. 45, no. 4, pp. 675–686, 2000.

[31] F. Altpeter, "Friction modeling, identification and compensation," Ph.D. dissertation, Ecole Polytechnique Federale de Lausanne, 1999 [Online]. Available:http://biblion.epfl.ch/EPFL/theses/1999/1988/EPFL_TH1988.pdf.

[32] S.L. Lacy, D.S. Bernstein, and S.P. Bhat, "Hysteretic systems and step-convergent semistability," in *Proc. American Control Conf.*, Chicago, IL, June 2000, pp. 4139–4143.

AUTHOR INFORMATION

Ashwani K. Padthe received the bachelor's degree in aerospace engineering from the Indian Institute of Technology Bombay in 2003. In 2006 he received the M.S. in aerospace engineering at the University of Michigan, where he is now pursuing the Ph.D. His research interests include hysteretic systems and aeroelasticity.

Bojana Drincic received the bachelor's degree in aerospace engineering from the University of Texas at Austin in 2007. She is now pursuing a Ph.D. at the University of Michigan. Her research interests include hysteretic systems, systems with friction, and spacecraft dynamics and control.

JinHyoung Oh received the bachelor's degree in control and instrumentation engineering from Korea University and master's degrees in aerospace engineering and applied mathematics from Georgia Institute of Technology. He received the Ph.D. in aerospace engineering from the University of Michigan in 2005. He is currently employed by AutoLiv as a research engineer.

Demosthenis D. Rizos received the diploma in mechanical engineering from the University of Patras in 1999, where he is a doctoral candidate. His research interests are in experimental modal analysis, identification of linear and nonlinear mechanical systems, systems with friction, and fault detection and identification. He has contributed to several sponsored research projects and is a coauthor of more than 15 publications.

Spilios D. Fassois received the diploma in mechanical engineering from the National Technical University of Athens, Greece, in 1982, and the Ph.D. in mechanical engineering from the University of Wisconsin-Madison in 1986. He served on the faculty of the Department of Mechanical Engineering and Applied Mechanics of the University of Michigan from 1986 to 1994 and is currently on the faculty of the Department of Mechanical and Aeronautical Engineering of the University of Patras, Greece. His research interests are in the area of stochastic mechanical systems, including vibrating systems, with an emphasis on identification and fault detection. He leads the Stochastic Mechanical Systems and Automation (SMSA) Laboratory at the University of Patras and is the author of more than 130 publications. His research has been supported by Ford, Eastman Kodak, General Motors, Whirlpool, Hellenic Aerospace, Hellenic Railways, Alenia, BAE Systems, and Volkswagenstiftung. He is a member of the editorial board of the *Journal of Mechanical Systems and Signal Processing*, and he was a guest editor for the special section on system identification in the October 2007 issue of *IEEE Control Systems Magazine*.

Dennis S. Bernstein (dsbaero@umich.edu) is a professor in the Aerospace Engineering Department at the University of Michigan. He is editor-in-chief of *IEEE Control Systems Magazine* and the author of *Matrix Mathematics* (Princeton University Press). His interests are in system identification and adaptive control for aerospace applications. He can be contacted at the University of Michigan, Aerospace Engineering Department, 1320 Beal Ave., Ann Arbor, MI 48109-2140 USA.